

---


Retrospective Theses and Dissertations

---

1991

## Photorefractive Materials for Optical Signal Processing

William B. Lawler  
*University of Central Florida*

 Part of the [Electrical and Computer Engineering Commons](#)  
Find similar works at: <https://stars.library.ucf.edu/rtd>  
University of Central Florida Libraries <http://library.ucf.edu>

This Masters Thesis (Open Access) is brought to you for free and open access by STARS. It has been accepted for inclusion in Retrospective Theses and Dissertations by an authorized administrator of STARS. For more information, please contact [STARS@ucf.edu](mailto:STARS@ucf.edu).

---

### STARS Citation

Lawler, William B., "Photorefractive Materials for Optical Signal Processing" (1991). *Retrospective Theses and Dissertations*. 3865.  
<https://stars.library.ucf.edu/rtd/3865>

PHOTOREFRACTIVE MATERIALS  
FOR OPTICAL SIGNAL PROCESSING

BY

WILLIAM B. LAWLER  
B.A., Hampden-Sydney College, 1975  
B.S.E.E., Old Dominion University, 1989

THESIS

Submitted in partial fulfillment of the requirements  
for the degree of  
Master of Science in Electrical Engineering  
in the Graduate Studies Program  
of the College of Engineering  
University of Central Florida  
Orlando, Florida

Spring Term  
1991

## ABSTRACT

The optical response of the photorefractive crystals  $\text{KNbO}_3:\text{Ta}$ ,  $\text{KNbO}_3:\text{Fe}$ ,  $\text{LiNbO}_3:\text{Fe}$ , and nominally pure  $\text{BaTiO}_3$  is investigated. In the experiment, a holographic grating is built in the crystal under investigation via a two-wave mixing scheme that utilizes the signal-processing capacities of two acousto-optic Bragg cells. The dynamic interaction of the Bragg cells with the photorefractive grating causes a heterodyned RF signal to appear on the output laser beam, enabling the real-time, direct measurement of the amplitude and phase of the space-charge fields in the crystal. Experimental results are presented for the amplitude and phase of the space-charge fields, the diffraction efficiency, and the grating time constant as a function of spatial frequency.

Quantitative understanding of some of the fundamental processes and material properties responsible for the optical response is gained through comparison of the measured data to theoretical models. In this analysis, the diffusion and photovoltaic transport lengths, Debye screening length, net trap concentration, and net conductivity factor are determined.

## ACKNOWLEDGEMENTS

I wish to express thanks to several people for their help and support in the completion of this project. First to Jim Moharam, whose creativity, enthusiasm, patience, and understanding have been a source of motivation. Chris Sherman, whose thesis on the implementation of the optical correlator is referenced at the end of this paper, shared his technical expertise and volunteered for often lengthy data runs, and Don Gray provided help with data acquisition. The help rendered by Marc Himel in the eleventh hour printing of the thesis is appreciated. Warm thanks go to my mother and father for their continual support and encouragement. Also, I wish to thank Dr. Wassail for his sound advice on the subject of creative thinking.

This research was supported in part by the Florida High Technology Industrial Council and the Electronics Systems Sector at Harris Corporation. Dr. J.J. Kim provided the barium titanate crystal. The experimental work was performed at the Center for Research in Electro-Optics and Lasers (CREOL).

## TABLE OF CONTENTS

LIST OF FIGURES .....	v
LIST OF TABLES .....	vi
LIST OF VARIABLES .....	vii
INTRODUCTION .....	1
ACOUSTO-OPTICS .....	3
PHOTOREFRACTION .....	8
The Linear Electro-Optic Effect in Anisotropic Media .....	8
Development of the Photorefractive Field .....	11
EXPERIMENTAL CONFIGURATION .....	19
Background .....	19
Qualitative Discussion of the Measurement System .....	21
FIELD ANALYSIS OF THE EXPERIMENTAL SYSTEM .....	28
Signal Creation and Grating Formation .....	28
Field Analysis at the Detector .....	34
EXPERIMENT .....	40
Testing .....	40
Experimental Results for BaTiO <sub>3</sub> .....	44
Experimental Results for KNbO <sub>3</sub> :Ta .....	48
Experimental Results for LiNbO <sub>3</sub> :Fe .....	50
Experimental Results for KNbO <sub>3</sub> :Fe .....	53
DETERMINATION OF MATERIAL PROPERTIES .....	57
Analytic Methods .....	57
Material Properties .....	59
Summary .....	63
REFERENCES .....	64

## LIST OF FIGURES

Figure 4.1 Experimental Configuration for $\Lambda=1.5$ and $\Lambda=2.5 \mu\text{m}$ . . . . .	22
Figure 4.2 Experimental Configuration for $\Lambda=10.5 \mu\text{m}$ . . . . .	23
Figure 5.1 Wavevector Diagram for Bragg Cell #1 . . . . .	29
Figure 5.2 Wavevector Diagram for Bragg Cell #2 . . . . .	32
Figure 5.3 Wavevector Diagram for the Photorefractive Crystal . . . . .	35
Figure 6.1 Measured Amplitude and Phase Data KNbO <sub>3</sub> :Ta, $I=100 \text{ mW/cm}^2$ , $\Lambda=2.5 \mu\text{m}$ . . . . .	41
Figure 6.2 Amplitude and Phase of the Space-Charge Field from the data of Figure 6.1 . . . . .	43
Figure 6.3 Amplitude and Phase of the Space-Charge Fields in BaTiO <sub>3</sub> as a Function of Spatial Frequency . . . . .	45
Figure 6.4 Diffraction Efficiency and $\Delta n$ in BaTiO <sub>3</sub> , $\Lambda=1.5 \mu\text{m}$ . . . . .	48
Figure 6.5 Amplitude and Phase of the Space-Charge Fields in KNbO <sub>3</sub> :Ta as a Function of Spatial Frequency . . . . .	49
Figure 6.6 Amplitude and Phase of the Space-Charge Fields in LiNbO <sub>3</sub> :Fe as a Function of Spatial Frequency . . . . .	51
Figure 6.7 Amplitude and Phase of the Space-Charge Fields in KNbO <sub>3</sub> :Fe as a Function of Spatial Frequency . . . . .	54
Figure 7.1 Comparison of Experimental Data and Theoretical Model for BaTiO <sub>3</sub> as a Function of Spatial Frequency. . . . .	61
Figure 7.2 Comparison of Experimental Data and Theoretical Model for KNbO <sub>3</sub> :Ta as a Function of Spatial Frequency . . . . .	62

## LIST OF TABLES

TABLE 6.1	MATERIAL PARAMETERS FOR THE PHOTOREFRACTIVE CRYSTALS .....	44
TABLE 6.2	MEASURED FIELD PARAMETERS FOR BaTiO <sub>3</sub> .....	46
TABLE 6.3	MEASURED FIELD PARAMETERS FOR KNbO <sub>3</sub> :Ta .....	50
TABLE 6.4	MEASURED FIELD PARAMETERS FOR LiNbO <sub>3</sub> :Fe .....	53
TABLE 6.5	MEASURED FIELD PARAMETERS FOR KNbO <sub>3</sub> :Fe .....	55
TABLE 7.1	MATERIAL PROPERTIES .....	60

## LIST OF VARIABLES

$p$	strain-optic tensor
$S$	strain-field strength
$\omega$	angular frequency
$\mathbf{K}$	grating wave vector
$v$	velocity
$\Lambda$	spatial period
$I$	intensity
$\rho$	mass density
$\mathbf{k}$	optical wave vector
$\lambda$	optical wavelength
$\theta_B$	Bragg angle
$d$	grating thickness
$Q$	grating parameter
$\eta$	diffraction efficiency
$\gamma$	grating strength
$\epsilon$	permittivity
$n$	refractive index
$r$	electro-optic coefficient
$E$	electric field



$q$	electronic charge
$\mu$	carrier mobility
$D$	diffusion coefficient
$n(z,t)$	carrier concentration
$J$	current density
$\kappa$	photovoltaic material constant
$\alpha$	absorption coefficient
$\phi_{ph}$	photovoltaic phase
$L$	carrier transport length
$g$	carrier generation rate
$\tau$	carrier lifetime
$N$	impurity concentration
$l_s$	Debye screen length
$F$	fractional poling factor
$\bar{\sigma}$	net conductivity factor
$\psi$	dephasing parameter
$\phi$	photorefractive phase

## CHAPTER 1

### INTRODUCTION

The real-time processing of information by coherent optical systems demands materials which possess high photosensitivity, good dynamic range, diffraction efficiency and spatial resolution. The process of crystal fabrication and introduction of the dopant necessary for building a photorefractive grating is somewhat empirical, with the optical properties varying as a function of the techniques and materials employed. More exacting characteristics may be required for particular applications. Photorefractive materials, as fabrication methods and characterization techniques improve, are finding extensive applications in optical signal processing systems as well as dynamic holography, phase conjugation and image storage. This thesis is motivated by the need for experimental determination of the optical characteristics of photorefractive crystals for optical correlation and optical adaptive filtering systems.

The photorefractive crystals iron-doped lithium niobate ( $\text{LiNbO}_3:\text{Fe}$ ), iron-doped potassium niobate ( $\text{KNbO}_3:\text{Fe}$ ), nominally pure barium titanate ( $\text{BaTiO}_3$ ), and tantalum-doped potassium niobate ( $\text{KNbO}_3:\text{Ta}$ ) are characterized for optical response. The experimental system was built around an existing acousto-optic correlator which uses a photorefractive crystal as the integrating element. This system is the result of the collaboration of Robert Montgomery and Mike Lange of Harris Corporation, Jim Moharam, and other workers in this laboratory. This heterodyne system enables the real time, direct measurement of the amplitude and phase of photorefractive gratings.

Chapter 2 highlights the theoretical foundations of acousto-optic diffraction applicable to this work. In Chapter 3, models of the development of photorefractive fields are shown, and several factors influencing the formation of a photorefractive phase grating are discussed. A qualitative description of the experimental configuration, components, electronics and rationale for such is given in Chapter 4. This is followed in Chapter 5 with a field analysis of the optical signal as it passes through the experimental system. Experimental results and grating characteristics are presented in Chapter 6 along with a discussion of the results and the performance of the measurement system. In Chapter 7, the experimental results are analyzed and material properties calculated from the measured data are presented.

## CHAPTER 2

### ACOUSTO-OPTICS

Acousto-optics is the field dealing with the interaction of optical waves and acoustic waves. Until the advent of the laser the field was predominately academic, with few applications. Because photons have no charge, making optical beams somewhat difficult to control, acousto-optic devices have found applications in beam deflectors, modulators, tunable optical filters, spectrum analyzers, and various signal-processing systems.

Two acousto-optic Bragg cells are used in the experimental system. The first is a glass cell used for signal modulation, while the second is made of tellurium dioxide ( $\text{TeO}_2$ ) and is used for beam deflection. In an acousto-optic cell, a sound wave is introduced into the cell via a piezo-electric transducer, creating a moving phase grating. Part of an optical beam incident on the cell is diffracted, with the diffraction efficiency increasing as a function of applied power, while the non-diffracted part passes through with diminished amplitude. The optical frequency of the diffracted wave undergoes a Doppler shift due to the motion of the grating. The following discussion presents the salient points of this process as outlined in Yariv and Yeh [1].

A propagating acoustic wave has the effect of a traveling pressure wave, creating a strain field within the medium and causing a periodic change in the refractive index. This phenomenon is known as the photoelastic effect, with the coupling between the refractive index and the acoustic wave represented by the strain-optic tensor  $p_{ij}$ . The crystalline

structure of TeO<sub>2</sub> is tetragonal, while glass is isotropic. For simplicity, the specific model discussed here applies to the case of isotropic materials, but the basic concepts are valid for both Bragg cells. Compensation for this and other differences between the two cells will be discussed in Chapter 4. The refractive index of a material perturbed by a sound wave traveling in the z-direction is given by [1],

$$n(z) = n - \frac{1}{2} n^3 p_{33} S_z \sin(\omega_a t - K_a z), \quad (2.1)$$

for beam polarization in the z-direction (horizontal), which can be assumed throughout the experimental system unless noted otherwise. In equation (2.1),  $n$  is the bulk refractive index,  $S$  is the strength of the strain field, and  $\omega_a$  is the angular frequency of the electrical signal driving the cell. The rightmost term in equation (2.1) is  $\Delta n$ , the change in refractive index.  $K_a$ , the spatial frequency of the acoustic wave, is defined by

$$K_a = \frac{\omega_a}{v_a} = \frac{2\pi}{\Lambda_a}, \quad (2.2)$$

where  $v_a$  is the velocity of the sound wave and  $\Lambda_a$  is the grating period. It can be seen that, for a given acoustic velocity, the grating period is inversely proportional to the driving frequency. The velocity  $v_a$  for the glass Bragg cell is 4,000 m/s and, typically, the driving frequency was about 70 MHz, giving a grating period  $\Lambda_a$  of about 50  $\mu\text{m}$ . For the TeO<sub>2</sub> cell  $v_a$  is 618 m/s, corresponding to  $\Lambda_a$  of about 9  $\mu\text{m}$  [2]. The strain field strength  $S$  is related to the RF input power by

$$S = \left( \frac{2I_a}{\rho_m v_a^2} \right)^{\frac{1}{2}}, \quad (2.3)$$

$I_a$  being the acoustic intensity, which is roughly equal to the RF input power divided by the contact area of the piezo-electric transducer [3]. In equation (2.3),  $\rho$  is the mass density of the medium. As the wave moves across the cell the acoustic power is attenuated. There is also attenuation as a function of vertical distance from the center of the cell, perpendicular to the wave motion. In this experiment, it is desired that the diffracted and transmitted beams have similar profiles. In order to maximize diffraction efficiency and retain similar profiles, it is necessary to use a small optical beam and center it near the transducer.

For an optical beam incident on the A-O cell, the relationship between the incident and diffracted wave vectors  $\mathbf{k}_i$  and  $\mathbf{k}_d$  for strong diffraction is given by [4]

$$\vec{\mathbf{k}}_d = \vec{\mathbf{k}}_i \pm \vec{\mathbf{K}}_a. \quad (2.4)$$

The angular frequency  $\omega_d$  of the diffracted beam is related to that of the incident beam by

$$\omega_d = \omega_i \pm \omega_a. \quad (2.5)$$

In equations (2.4) and (2.5) the plus sign is used when the Z-component of the optical and acoustic waves travel toward each other (phonon annihilation model) and the minus sign applies for waves with Z-components in the same direction (phonon creation model). Since the RF frequency  $\omega_a$  is much less than the optical frequency, its effect on  $\mathbf{k}_d$  in equation (2.4) may be ignored, leading to the Bragg equation for strong diffraction,

$$2n\Lambda \sin\theta_B = m\lambda, \quad (2.6)$$

where  $\lambda$  is the optical wavelength and  $m$  is an integer. Equation (2.6) predicts the angles of diffracted beams for an unslanted grating, given a beam incident at the Bragg angle  $\theta_B$ , which is the case in the experimental system. While the Doppler shift is insignificant in

calculating the Bragg angle, its effect on the frequency  $\omega_d$  will be very useful for signal processing purposes in the experimental system (Chapter 5).

For the purpose of modeling diffraction efficiency, diffraction gratings, both moving and stationary, are classified as "thick" (long interaction length  $d$ ) or "thin" (short interaction length). Two parameters,  $\rho$  [5] and  $Q$  [1], are defined to delineate the two regimes,

$$\rho = \frac{\lambda^2}{L^2 n \Delta n} \quad Q = \frac{2\pi \lambda d}{n \Lambda^2}. \quad (2.7)$$

If  $Q \ll 1$ , the grating is considered thin and the Raman-Nath equations describe the diffraction.  $\rho \gg 1$  denotes a thick grating, described by Bragg regime equations. Although neither of the Bragg cells satisfies the requirement  $Q \ll 1$  for the Raman-Nath regime, a brief discussion of Raman-Nath diffraction is included here because a stationary magnesium fluoride ( $\text{MgF}_2$ ) grating sputtered on glass is used as a beam splitter in the experimental system (Figure 4.1, page 25) and does operate in the Raman-Nath regime.

In equation (2.6),  $m$  is defined simply as an integer, implying that an infinite number of diffracted orders are possible. For practical purposes, in the Raman-Nath regime there can be many diffracted orders of significant intensity. The diffraction efficiency  $\eta_m$  of the  $m^{\text{th}}$  diffracted order for a beam normally incident is given by the Bessel functions [1]

$$\eta_m = J_m^2\left(\frac{2\pi \Delta n d}{\lambda}\right). \quad (2.8)$$

For the Raman-Nath regime, the maximum diffraction efficiency of any order is 33.8%, which occurs when  $m = \pm 1$ . The diffraction efficiency of the  $\text{MgF}_2$  grating is about 4% for each  $\pm 1$  diffracted order.

Both of the Bragg cells in the experimental system operate, appropriately, in the Bragg regime. In the Bragg regime there is only one significant diffracted order ( $m = \pm 1$ ) for a beam incident at the Bragg angle. The diffraction efficiency is expressed by [4]

$$\eta = \sin^2 \left[ \frac{\pi d n^3 p}{\lambda} \left( \frac{I_a}{2 \rho_m v_a^2} \right)^{\frac{1}{2}} \right] = \sin^2(\gamma_a). \quad (2.9)$$

The argument of the sine function in equation (2.9) is referred to as the acoustic grating strength  $\gamma_a$ . Since  $I_a$  is proportional to the RF power, equation (2.9) shows that the diffraction efficiency of the Bragg cell is controlled directly by the RF power. Also, by equations (2.2), (2.4), (2.5), and (2.6), the Bragg deflection angle and the magnitude and sign of the Doppler shift are controlled with the frequency of the driving signal.

It is clear that Bragg cells can be valuable devices for a variety of needs. The performance of the two Bragg cells and the interaction between them are critical factors in the signal-processing and beam configuration aspects of the experiment. The experimental system essentially is built around these two A-O devices. The concepts and relationships presented in this chapter will be seen again in the system model.



## CHAPTER 3

### PHOTOREFRACTION

When light of a suitable wavelength propagates through a photorefractive crystal, charge carriers are ionized from impurity sites, enabling their travel through the lattice until trapping occurs some distance away, normally in the nanometer range. This process of freeing and trapping carriers may continue until the carrier has migrated out of the illuminated region. In the dark, depending on the crystal type and dopant, the charge carrier can remain trapped, with no fixing process, for a time ranging from milliseconds to months. This redistribution of charge leaves a non-zero net charge concentration in both the illuminated and dark regions, one positive and one negative, creating a space-charge field that influences further carrier migration. As more charge carriers migrate toward the dark regions, the space-charge field gains strength and more strongly influences carrier migration. Eventually, a steady-state condition exists in which there is no net charge transport. The space-charge field induces a change in the refractive index via the electro-optic effect.

#### The Linear Electro-Optic Effect in Anisotropic Media

The electro-optic effect is defined as the dependence of the index of refraction on an applied electric field. All materials are subject to this effect, but in only a select few is the response great enough for practical application. In anisotropic crystals, the dielectric response is non-scalar and is expressed in terms of the dielectric permittivity tensor  $\epsilon_{ij}$ , in the notation of Yariv and Yeh [1], as

$$D_i = \epsilon_{ij} E_j, \quad (3.1)$$

with summation over repeated indices.  $D$  is the electric displacement and  $E$  is the electric field. In terms of the principal optical axes of the crystal, the effect of an applied electric field is incorporated into the impermeability tensor,

$$\frac{1}{\epsilon} = \frac{1}{\epsilon_o} \begin{bmatrix} \frac{1}{n_x^2} & 0 & 0 \\ 0 & \frac{1}{n_y^2} & 0 \\ 0 & 0 & \frac{1}{n_z^2} \end{bmatrix} + \frac{1}{\epsilon_o} \begin{bmatrix} \Delta\left(\frac{1}{n^2}\right)_1 & \Delta\left(\frac{1}{n^2}\right)_6 & \Delta\left(\frac{1}{n^2}\right)_5 \\ \Delta\left(\frac{1}{n^2}\right)_6 & \Delta\left(\frac{1}{n^2}\right)_2 & \Delta\left(\frac{1}{n^2}\right)_4 \\ \Delta\left(\frac{1}{n^2}\right)_5 & \Delta\left(\frac{1}{n^2}\right)_4 & \Delta\left(\frac{1}{n^2}\right)_3 \end{bmatrix}, \quad (3.2)$$

where  $n_x$ ,  $n_y$ , and  $n_z$  are the refractive indices for the appropriate subscripted directions. The first term on the right-hand side is the zero-field state, and the second term accounts for the effect of an applied field. The relation between the change in index and the applied field is given by

$$\Delta\left(\frac{1}{n^2}\right)_i = r_{ij} E_j, \quad (3.3)$$

where the  $r_{ij}$  are the linear, or Pockels, electro-optic coefficients for the material. The Pockels coefficients have been determined experimentally for many crystal types, including the ones investigated here, and are published in several sources [1,6,7,9].

Using the above relations and energy density arguments, Yariv and Yeh present an index ellipsoid equation which characterizes wave propagation in the presence of an electric field for the case of a uniaxial crystal. The crystals  $\text{LiNbO}_3\text{:Fe}$ ,  $\text{BaTiO}_3$ ,  $\text{KNbO}_3\text{:Ta}$ , and

KNbO<sub>3</sub>:Fe are all uniaxial, having only two principal indices, namely  $n_o$  and  $n_e$ . In the experiment, a crystal under investigation is aligned so that the c-axis points in the z-direction (horizontal). For this orientation, the index ellipsoid equation is given by

$$\left(\frac{1}{n_o^2} + r_{1k}E_k\right)x^2 + \left(\frac{1}{n_o^2} + r_{2k}E_k\right)y^2 + \left(\frac{1}{n_e^2} + r_{3k}E_k\right)z^2 + 2yzr_{4k}E_k + 2xzr_{5k}E_k + 2xyr_{6k}E_k = 1, \quad (3.4)$$

where  $k=1,2,3$ . In the experimental configuration, neither the space-charge field within the photorefractive crystal nor the electric field of the laser beam has a component in the y-direction, and the wave vectors of the beams entering the crystal are contained in the x-z plane. These considerations allow simplification of the above index ellipsoid equation to

$$\left(\frac{1}{n_o^2} + r_{1k}E_k\right)x^2 + \left(\frac{1}{n_e^2} + r_{33}E_z\right)z^2 + 2xzr_{5k}E_k = 1, \quad (3.5)$$

with the optic axis of the crystal in the z-direction. Experimentally, there was no case in which the x-component of the electric field vectors in a crystal were greater than .5% of the total field. Although the investigated crystals have different electro-optic tensors, insertion of the E-O tensor for each crystal into equation (3.5) and consideration of the small field components in the x-direction leads to a single index ellipsoid equation for all four crystals,

$$\left(\frac{1}{n_e^2} + r_{33}E_z\right)z^2 = 1. \quad (3.6)$$

Accordingly, the refractive index change due to the presence of a field within the photorefractive crystals is modeled by

$$\Delta n = -\frac{1}{2} n_e^3 r_{33} E_z. \quad (3.7)$$

### Development of the Photorefractive Field

As will be seen in Chapter 5, a sinusoidal intensity pattern in the crystal under investigation is used to induce grating formation. In illuminated regions, photoionization frees charge carriers from trap sites within the bandgap, enabling their migration toward dark regions. There are several valence states for each trap. In most models, two valence states are assumed to participate in the trapping process. For example, in  $\text{LiNbO}_3:\text{Fe}$  the donor and acceptor states are generally accepted as  $\text{Fe}^{2+}$  and  $\text{Fe}^{3+}$  [8], respectively, indicating that electrons are assumed to be the charge carriers. The valence states for the  $\text{KNbO}_3:\text{Fe}$ ,  $\text{BaTiO}_3$ , and  $\text{KNbO}_3:\text{Ta}$  crystals are not known to this author. In general, the charge carriers can be electrons, holes, or both. The dominant carrier is dependent on the material, the dopant, the spatial frequency, the dopant concentration, the method of crystal fabrication, and the relative concentrations of donors and acceptors [6,9]. The latter three parameters are not known for these crystals. For  $\text{BaTiO}_3$ , the identity of the impurity at the trap sites is unknown also. In any event, one carrier must dominate for a photorefractive grating to be formed. The uncertainty regarding the actual charge carriers can be circumvented at the device level by assuming the conductivity  $\sigma$  to be a net conductivity [8,10]. Henceforth, in the development of field equations, electrons will be

assumed to be the dominant carriers and a net conductivity factor will allow for both carriers.

Moharam, Gaylord, and Magnusson [11] have developed models for the transport of charge carriers and the formation of space-charge fields while imposing no restrictions on the carrier transport lengths. Three mechanisms for transport are defined: drift caused by applied or space charge field, diffusion, and the bulk photovoltaic effect. In the experiment there was no applied field. Allowing for these effects yields a current density within the crystal under illumination,

$$J(z,t) = qD \frac{\partial n(z,t)}{\partial z} + q\mu n(z,t)E_{sc}(z,t) + J_{ph}. \quad (3.8)$$

$E_{sc}$  is the space charge field,  $q$  is the electronic charge,  $\mu$  is the carrier mobility,  $D$  is the diffusion coefficient, and  $n(z,t)$  is the free carrier concentration.  $n(z,t)$  is the sum of two terms:  $n_L(z,t)$ , the photoinduced carrier concentration, and  $n_D(z,t)$ , the carrier concentration in the dark.  $J_{ph}$  is the anisotropic current attributed to the bulk photovoltaic effect,

$$J_{ph}(z) = -\kappa \alpha I_o \left( 1 + \frac{m}{[1 + (KL_{ph})^2]^{\frac{1}{2}}} \cos(Kz - \phi_{ph}) \right). \quad (3.9)$$

$\kappa$  is an empirical material constant and  $\alpha$  is the absorption coefficient.  $J_{ph}$  is proportional to the intensity pattern but is shifted spatially by the photovoltaic phase  $\phi_{ph}$ ,

$$\phi_{ph} = \tan^{-1}(KL_{ph}), \quad (3.10)$$

where the photovoltaic transport length  $L_{ph}$  is defined by

$$L_{ph} = \frac{\kappa \hbar \omega}{q \xi} . \quad (3.11)$$

$\hbar\omega$  is the photon energy, and  $\xi$  is the quantum efficiency. Note that the photovoltaic phase is dependent on the  $KL_{ph}$  product, not on either factor alone.

Moharam et al. use the continuity equation,

$$\frac{\partial n(z,t)}{\partial z} = g(z) - \frac{n(z,t) - n_D}{\tau} + \frac{1}{q} \frac{\partial J(z,t)}{\partial z} , \quad (3.12)$$

and Poisson's equation to solve for the space charge field for several exposure-time limits. In equation (3.12),  $g(z)$  is the carrier generation rate  $g_0 I(z)/I_0$ , and  $g_0 = \alpha \xi I_0 / \hbar \omega$ . The short-time limit model is applicable at the very start of grating formation, when the space charge field has not developed to the extent that it appreciably influences charge migration, and  $\partial n / \partial t = 0$ . In this short-time model, the slope of the space-charge field with respect to time is linear. The space-charge field for this model is

$$E_{sc}(z,t) = \frac{q g_0 t m}{\epsilon [1 + (KL_{ph})^2]^{1/2}} \left[ L_{ph} \cos(Kz - \phi_{ph}) + \frac{KL_D^2}{1 + (KL_D)^2} \sin(Kz - \phi_{ph}) \right] , \quad (3.13)$$

where  $L_D$  is the transport length for diffusion,

$$L_D = (\tau D)^{\frac{1}{2}} , \quad (3.14)$$

$\tau$  is the free carrier lifetime, and  $m$  is the modulation factor

$$m = \frac{2(I_1 I_2)^{\frac{1}{2}}}{I_1 + I_2}. \quad (3.15)$$

$I_1$  and  $I_2$  are the intensities of the two input beams. Equation (3.13) is the general equation for the space charge field applicable to the experimental configuration in the short-time limit.

For a diffusion-dominated field, equation (3.13) reduces to

$$E_{sc}(z, t) = \frac{q g_o t m}{\epsilon} \frac{K L_D^2}{[1 + (K L_D)^2]} \sin(Kz). \quad (3.16)$$

When the photovoltaic effect dominates, equation (3.13) reduces to

$$E_{sc}(z, t) = \frac{q g_o t m}{\epsilon} \frac{L_{ph}}{[1 + (K L_{ph})^2]^{1/2}} \cos(Kz - \phi_{ph}). \quad (3.17)$$

It is noteworthy that, in equation (3.16), the phase of the diffusion field is  $90^\circ$ , independent of  $L_D$ , while the phase of the photovoltaic field, by equations (3.10) and (3.17), depends on  $K L_{ph}$ . In order to determine experimentally the fields responsible for the refractive index change, it is clear that the ability to measure accurately the phase of the space charge fields is critical.

In the saturation model  $\partial n / \partial t = 0$  and the current density is constant. The space-charge field limits carrier migration and the maximum field has been attained,

$$E_{sc}(z) = -2 E_e \left[ \left( \frac{1}{m_1^2} - 1 \right)^{\frac{1}{2}} - \frac{1}{m_1^2} \right] \cos(Kz - \phi_e), \quad (3.18)$$

where  $m_1$  is the effective grating modulation ratio  $m \tau g_o / (n_D + \tau g_o)$  and

$$E_e = \left( E'_D{}^2 + E'_v{}^2 \right)^{\frac{1}{2}}, \quad (3.19)$$

$$E'_D = \frac{Kk_B T}{q} + KL_{ph} E'_v, \quad (3.20)$$

and

$$E'_v = \frac{L_{ph}}{\mu \tau} \left[ 1 + (KL_{ph})^2 \right]. \quad (3.21)$$

$k_B$  is the Boltzmann constant and  $T$  is the temperature in degrees Kelvin. The phase  $\phi_e$  of the space-charge field with respect to the spatial light pattern is defined by

$$\phi_e = \tan^{-1} \left( \frac{E'_D}{E'_v} \right). \quad (3.22)$$

In the space-charge field expressions shown above for the saturation model, it is assumed that there are an unlimited number of traps available for carrier excitation and recombination. Both the total number of traps and the relative concentrations of the valence states participating in charge transport are important for determination of the net saturation field amplitude. It is a net amplitude that is measured at saturation. In reference [19], these two factors are combined into an effective trap concentration,  $N_T$ ,

$$N_T = \frac{NN^+}{N + N^+}, \quad (3.23)$$

where  $N$  and  $N^+$  are the concentrations of the two valence states assumed to exist at the trap site. When modeling the net field, the local interactions between individual charge carriers must be considered in addition to the bulk electrostatic effects of the space-charge field. A



model which incorporates local interactions is that of the Debye screen field  $E_q$ , which sets a limit on the maximum attainable net field for a given net trap concentration  $N_T$  [22],

$$E_q = \frac{qN_T}{\epsilon K}. \quad (3.24)$$

The effect of  $N_T$  can be likened to the equivalent resistance of two parallel resistors, where the maximum resistance is determined by the smaller resistor. Thus the population of the lessor-populated impurity valence state determines the maximum attainable space-charge field. A maximum in the net saturation field is reached when the grating spacing  $\Lambda$  is equal to the Debye screening length  $l_s$  [19],

$$l_s = \left( \frac{4\pi^2 \epsilon k_B T}{q^2 N_T} \right)^{\frac{1}{2}}. \quad (3.25)$$

The screening length is a theoretical radius around a charge carrier that defines interactions with other carriers. If two charge carriers are within a Debye radius of each other, the local, single particle interaction is strong, and may screen the influence of the space-charge field. If the distance is larger than the Debye radius, the effects of the space-charge field dominate.

It was mentioned earlier in the chapter that both electrons and holes may participate simultaneously in the charge transport process. This may result in electron-hole competition and reduce the magnitude of the space-charge field. The effect of the carrier competition is incorporated into the net conductivity factor  $\bar{\sigma}$  [19],

$$\bar{\sigma} = \frac{\mu_p p - \mu_n n}{\mu_p p + \mu_n n}, \quad (3.26)$$

where  $\mu_p$  and  $\mu_n$  are the hole and electron mobilities, and  $p$  and  $n$  are the hole and electron concentrations. Another factor contributing to the saturation value of the field is the fractional poling factor  $F$  [22], which arises due to incomplete poling during crystal manufacture. Combining the above considerations with work in reference [12] results in an expression for the net saturation value of the space-charge field that allows for the effects of Debye screening, net trap concentration, electron-hole competition, and incomplete poling,

$$E_{SC}(z) = F \bar{\sigma} E_q \left[ \frac{E'_v{}^2 + E'_D{}^2}{E'_v{}^2 + (E'_D + E_q)^2} \right]^{\frac{1}{2}} \cos(Kz - \phi), \quad (3.27)$$

where  $\phi$ , the phase of the photorefractive field at saturation, is given by

$$\phi = \tan^{-1} \left[ \frac{E'_D}{E'_v} \left( 1 + \frac{E'_D}{E_q} + \frac{E'_v{}^2}{E'_D E_q} \right) \right]. \quad (3.28)$$

Equations (3.27) and (3.28) will be used to model the saturation fields measured in the experiment.

At this point it is thought to be appropriate to comment on the spatial dependence of the field terms defined in the last few pages. In experiments of the kind done in this work with oxide crystals, the product of spatial frequency and transport length is usually much less than unity. It can be seen that, for small  $KL$ , the diffusion field is proportional to the spatial frequency, while the photovoltaic field has very little dependence on spatial frequency (equations (3.13), (3.20), and (3.21)). Also, by equation (3.10), the phase of the photovoltaic field should be close to  $0^\circ$ . For small transport lengths, the phase of a

diffusion-dominated field should be very close to  $90^\circ$ . When both fields are present, the phase moves toward  $90^\circ$  as the spatial frequency increases.

A simplified expression for the general time dependence of the amplitude of the space-charge field appears in reference [13], given by

$$E_{sc}(t) = E_{sc}(z) \left( 1 - e^{-\frac{t}{\tau_{eff}}} \right). \quad (3.29)$$

The effective time constant  $\tau_{eff}$  is useful for modeling the crystal response as well as serving as a basis of comparison for different crystals.  $\tau_{eff}$  accounts for the generation rate, the carrier drift, diffusion, and recombination times, and the dielectric relaxation time. Equation (3.29) will be used to model crystal response for exposure times that span the short-time and saturation limit models.

This chapter began with a brief description of the photorefractive effect. It was shown that illumination of a photorefractive crystal with a spatial light pattern may induce the formation of a phase grating via the electro-optic effect. Field models, in terms of transport lengths, were shown for two exposure-time limits. Finally, a field equation that models the general time dependence was given.

## CHAPTER 4

### EXPERIMENTAL CONFIGURATION

#### Background

This chapter begins with a summary of some of the measurement techniques used by others in related work, followed by a qualitative discussion of the experimental system used in this work. Diagrams of the experimental configuration are shown in Figures 4.1 and 4.2.

Historically, measurements of grating amplitude have been accomplished by beam coupling experiments [10,14,15,16,17,18,19] or by diffraction efficiency measurement techniques that employ a third beam to probe the grating [20,21,22]. The beam coupling technique for measuring amplitude depends on the spatial shift between the grating phase and the incident light pattern. Beam coupling between two beams writing a photorefractive grating occurs when the grating phase shift is non-zero, and is maximum at a shift of  $\pm \pi/2$ . Measurement of the energy transfer between beams gives information needed for calculation of the beam-coupling coefficient, and from this the amplitude of the space-charge field and the grating phase can be found. In the three beam technique, the photorefractive grating is built by the interference of two relatively strong write beams. The third beam, or read beam, of relatively weak intensity and usually from a laser having a longer wavelength, is directed into the crystal at the Bragg angle. Measurement of the intensity of the diffracted portion of the read beam allows for calculation of the diffraction

efficiency, grating strength and, with knowledge of the electro-optic coefficient of the material, the amplitude of the space-charge field.

Phase measurement techniques [14,15,18,23,24,25] have been less direct than those of grating amplitude. The difficulty in phase measurement has been the establishment of a reference phase. The general method has been to build a photorefractive grating by the usual means and then translate the crystal, forcing the spatial phase between the grating and the spatial light pattern to move through several  $2\pi$  cycles. During this phase activity beam coupling measurements are made, and when maximum beam coupling occurs the sum of the forced shift and the photorefractive shift is assumed to equal  $\pm\pi/2$ . Extrapolation of the beam coupling data back to the time just before the forced phase cycling began gives a measure of the phase of the grating. Recently, Zha et al [18] have shown an improvement to this technique by modulating the phase of one of the write beams to accomplish relative movement between the spatial light pattern and the established grating. This method avoids the instability and other problems caused by mechanical movement.

The measurement technique used in this experiment, based on the system presented in reference [26], is fundamentally different from the measurement techniques outlined above and represents a significant improvement in the ability to characterize the response of photorefractive materials. The amplitude and phase of the photorefractive gratings are measured directly, and a heterodyne detection scheme provides an excellent signal-to-noise ratio.

The balance of this chapter describes in words the experimental system and the measurement technique used to characterize photorefractive crystals. The field equations that model the experimental system will be developed in Chapter 5.

### Qualitative Discussion of the Measurement System

The two variations of the system configuration are shown in Figures 4.1 and 4.2 on the following two pages. The difference between the two configurations lies in the means of controlling the angles at which the two beams enter the crystal.

The "front end" of the system, composed of a beam telescope, a fixed  $\text{MgF}_2$  diffraction grating, and Bragg Cell #1, provides an intensity-modulated beam which propagates through the rest of the system. The horizontally polarized output of the single mode argon laser is compressed as it passes through the telescope. Recall from the discussion of Bragg cells in Chapter 2 that, for this application, small beams entering the Bragg cells are needed to ensure that the diffracted and transmitted beam profiles do not change significantly as the beams pass through the cells. The beam telescope gives a measure of control of the beam size at the Bragg cells and at the crystal. A beam reduction factor of 2.5 was found to serve well. The  $\text{MgF}_2$  transmission grating, with  $100 \mu\text{m}$  grating spacing, serves as a beamsplitter, and is aligned normal to the input beam so that the  $\pm 1$  diffracted orders are equal in intensity and symmetric about the zero transmitted order. Typically, the intensities of the  $+1$  and  $-1$  orders of the  $\text{MgF}_2$  grating are balanced within 1%. The output of the fixed grating is imaged into Bragg cell #1, which is also aligned normal to the zero order beam, by the second lens in the telescope. An amplified 70 MHz signal from the sweep oscillator drives Bragg cell #1, forming a moving grating via the photoelastic effect. The second lens of the telescope images the fixed grating onto the moving acoustic grating in the Bragg cell such that both the  $\pm 1$  orders from the fixed grating satisfy the Bragg phase matching condition,  $2n\Lambda\sin\theta_B = \pm\lambda$ . For Bragg cell #1 the Bragg angle is about  $.3^\circ$ . The grating period is about  $50 \mu\text{m}$ , requiring that the second lens of the telescope reduce the

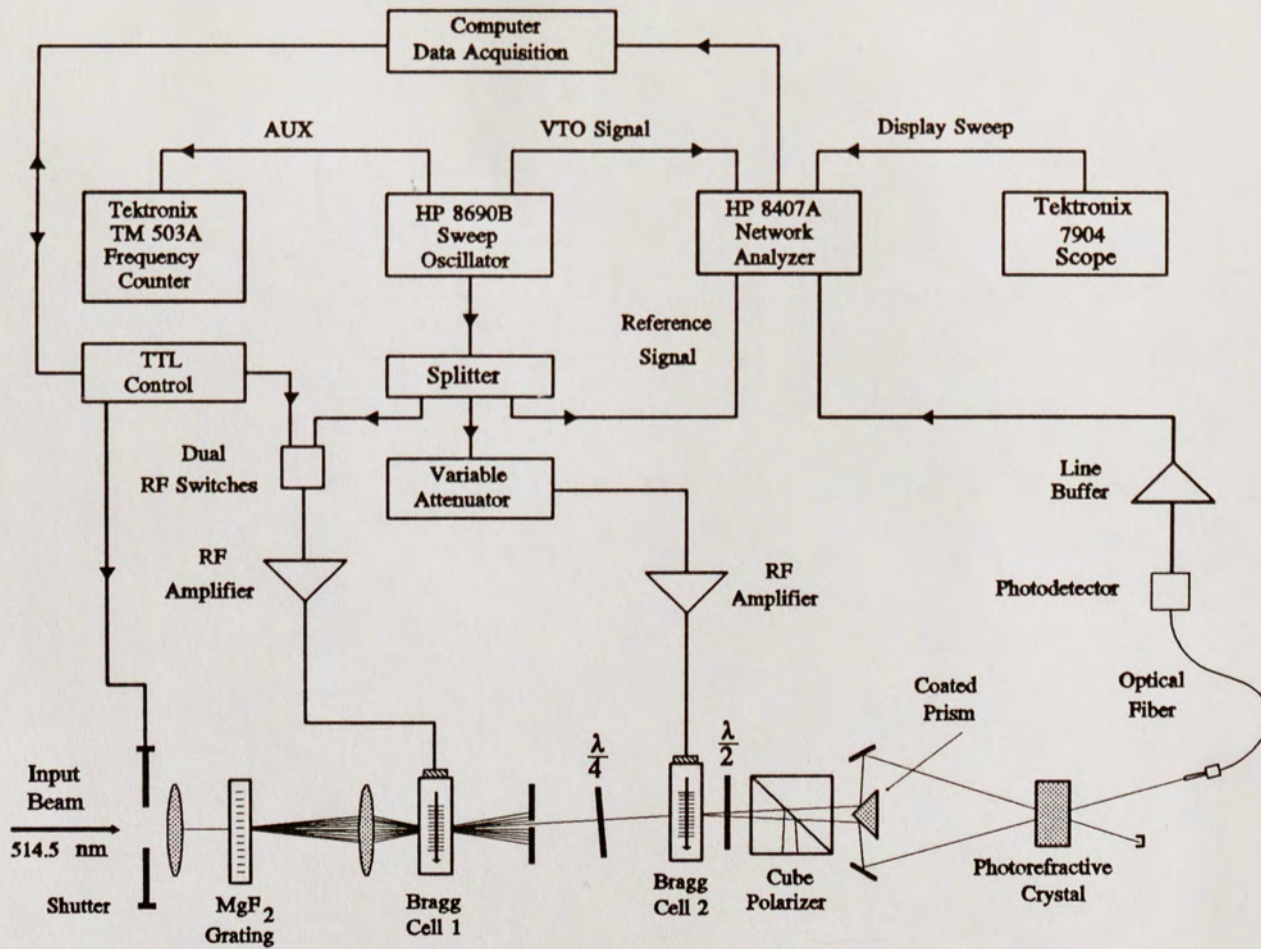


Figure 4.1 Experimental Configuration for  $\Lambda=1.5 \mu\text{m}$  and  $\Lambda=2.5 \mu\text{m}$

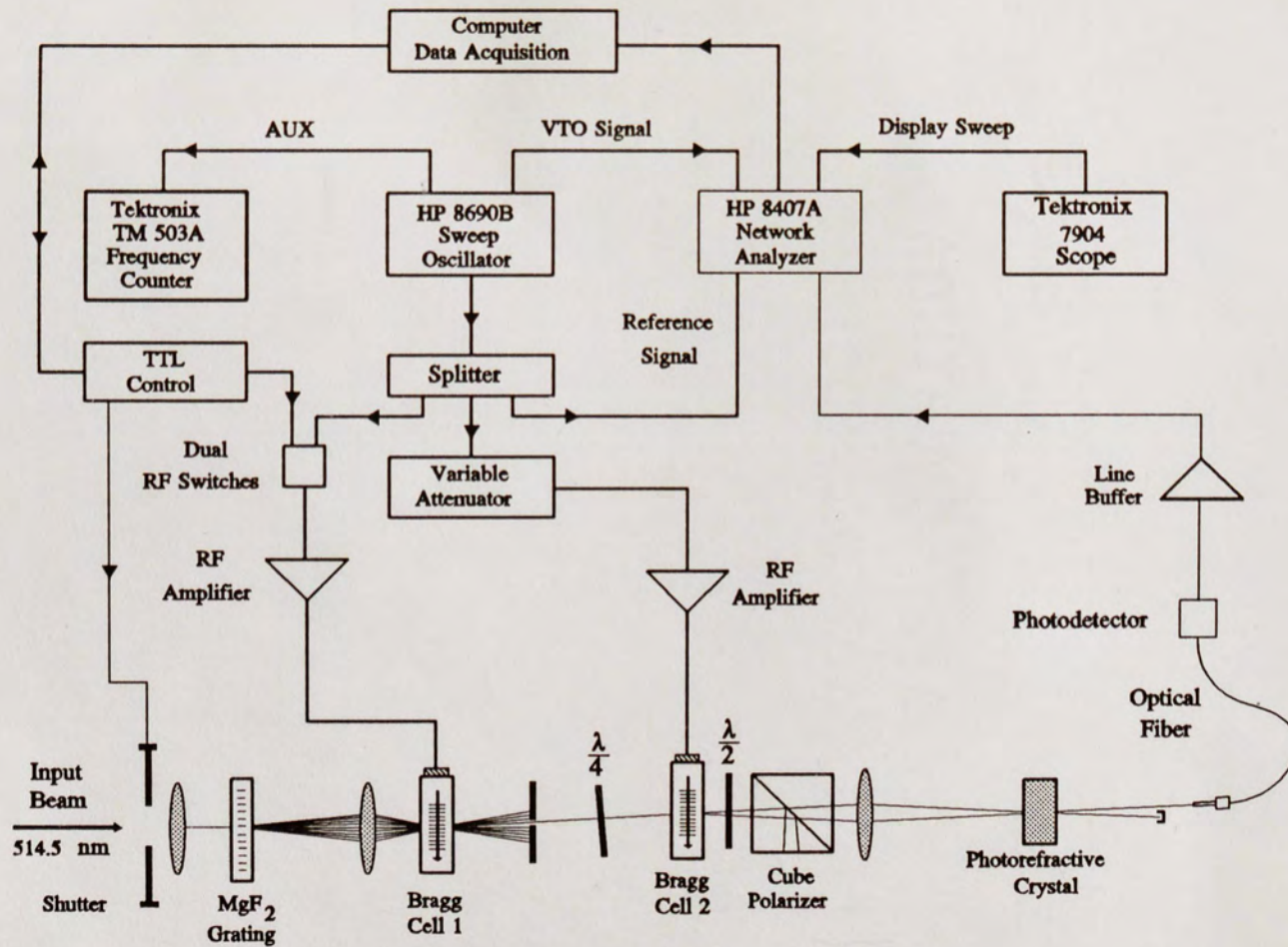


Figure 4.2 Experimental Configuration for  $\Lambda=10.5 \mu\text{m}$



image size of the  $\text{MgF}_2$  grating by a factor of about two. The  $\text{MgF}_2$  grating is mounted on a heavy translatable stage for fine-tuning of the image ratio.

Due to the proximity of the diffracted orders coming from the fixed grating, the zero order and some of the higher diffracted orders are allowed to enter Bragg cell #1, but only the  $\pm 1$  orders satisfy the Bragg condition. While passing through the acoustic grating, each  $\pm 1$  input beam is split into a transmitted beam and a Doppler-shifted, diffracted beam. The Doppler frequency shift is equal to the angular frequency  $\omega_{a1}$  of the RF signal driving the Bragg cell. Because of the symmetry of the input beams, the diffracted part of each input beam is exactly collinear with the transmitted part of the other. The result is a beat between the two beam components, modulating the beam intensity at the driving frequency  $\omega_{a1}$ . Typically, the RF power (about 25 dBm) driving the Bragg cell was adjusted for 50% diffraction efficiency, giving a signal modulation factor  $m \approx 1$ . Each output beam of the Bragg cell is intensity modulated, one due to a positive Doppler shift and the other due to a negative shift. In the experiment, the beam with an upshifted component was chosen for convenience.

It should be noted that other devices, such as electro-optic modulators, can be used to modulate the laser intensity; however, the Bragg cell holds several advantages. First, the Bragg cell serves as a bandpass filter for the driving RF power, effectively attenuating harmonics produced by the signal generator. Second, it produces a very clean frequency shift via the Doppler effect, as opposed to the Bessel dependence produced by an E-O modulator. Third, the Bragg cell is driven by an inexpensive, off the shelf RF amplifier, which reduces considerably RF pickup problems when compared to a high-voltage E-O driver.

The intensity-modulated beam from the front end is directed into Bragg cell #2, the TeO<sub>2</sub> cell, at the Bragg angle, where interaction with the acoustic grating splits the input beam into transmitted and diffracted beams. Bragg cell #2 is aligned such that the diffracted beam is shifted down in frequency, opposite to that of the first Bragg cell. Since both of the Bragg cells are driven by the same source, the magnitudes of the frequency shifts are equal. The TeO<sub>2</sub> cell is a rather singular device, and does not conform to the simple model discussed in Chapter 2. TeO<sub>2</sub> is optically active, and requires a circularly polarized input beam for maximum diffraction efficiency. The diffraction efficiency has sensitive dependence on input power, with the sensitivity increasing with power. On the optics bench, the input polarization requirement is accomplished through use of a quarter-wave plate, shown in Figures 4.1 and 4.2, which rotates the horizontal polarization beam arriving from the first Bragg cell. The polarizing beam splitter shown in the figures forces the horizontal polarization desired at the crystal. Also, it is desirable that the beams entering the crystal are of equal intensity for maximum contrast in the spatial light pattern. Recall that the diffraction efficiency of the  $\pm 1$  orders leaving the MgF<sub>2</sub> grating is only about 4%, meaning that over 90% of the incident intensity is lost at that device. Since only one of the output beams of Bragg cell #1 is used, at least 50% of the remaining intensity is lost there. The losses at the cube polarizer depend on the input polarization, and with circularly polarized input beams the power loss can be high. To alleviate this problem, a half-wave plate is located at the output of the TeO<sub>2</sub> cell. Through experimentation with the rotation angles of both the half and quarter-wave plates, an arrangement was reached in which the beams entering the crystal were of equal intensity and correct polarization at a tolerable power level in the TeO<sub>2</sub> cell. Because of the complexity of this arrangement, the configuration of the

quarter-wave plate,  $\text{TeO}_2$  cell, half-wave plate, and cube polarizer are modeled as a single device, referred to as Bragg cell #2. The transfer characteristics used for Bragg cell #1 are used to model both A-O devices. Experimentation has shown this to be a valid model. The advantage of the  $\text{TeO}_2$  cell is the large deflection angle of about  $1.7^\circ$ , which is desirable in both experimental configurations. More detailed information regarding  $\text{TeO}_2$  cells may be found in references [27,28,29].

For the case of Figure 4.1, the diffracted and transmitted beams leaving Bragg cell #2 are separated further by a reflection-coated prism and directed into the photorefractive crystal under investigation by mirrors  $M_1$  and  $M_2$ . This arrangement was used for fringe spacings  $\Lambda=1.5$  and  $\Lambda=2.5 \mu\text{m}$ . For the case of Figure 4.2, a positive lens images the acoustic grating in Bragg cell #2 into the crystal. This configuration was used for the  $10.5 \mu\text{m}$  grating spacing. The prism setup of Figure 4.1 allows for much greater control of the fringe spacing of the photorefractive grating and is considered to be the superior arrangement.

The two coherent beams from Bragg cell #2 interfere at the crystal to generate a spatial light pattern that builds the photorefractive grating. The two beams that write the grating are diffracted by it in a dynamic process as they pass through the crystal. Each output beam is composed of a transmitted component that has passed directly through the crystal and a diffracted component from the other beam. The symmetry of the beam configuration at the crystal is similar to that of the first Bragg cell, where two beams incident at the Bragg angle pass through a grating. At the output, transmitted and diffracted components overlap. Because of the Doppler shift from Bragg cell #2, the diffracted and transmitted components of each crystal output beam differ in frequency, creating a beat

between the two components at the RF frequency. The components diffracted by the grating acquire the phase of the spatial light pattern plus the photorefractive shift  $\phi$ .

One of the beams leaving the crystal is monitored by a high-speed photodetector, the output of which is fed into a network analyzer tuned to the driving RF frequency (bandwidth 10 kHz). The detector is isolated from the RF radiation on the optics bench by use of a multimode optical fiber. In the network analyzer the amplitude and phase of the signal from the detector are continuously compared to those of the reference signal (the RF driving signal). The output of the network analyzer, linear phase data and log of amplitude, is digitized for analysis via an analog-to-digital interface board installed in the computer.

During an experimental run, the RF power driving Bragg cell #1 is periodically switched off for a short time to interrupt the writing of the grating. The time when the modulation is off is referred to as the read period. This periodic switching produces a series of write-read cycles in the detected signal. The acquired data undergo straightforward numerical processing in order to obtain the amplitude and phase of the photorefractive space-charge field. The amplitude difference between the read and write signals is proportional to the strength of the photorefractive grating. The difference in phase between the read and write signals is  $\phi + \pi/2$ .

The measurement system discussed here gives direct, real-time information for the amplitude and phase of the photorefractive fields. Also, as opposed to the phase measurement techniques mentioned earlier in the chapter, this technique is nondestructive.

## CHAPTER 5

### FIELD ANALYSIS OF THE EXPERIMENTAL SYSTEM

In this chapter, field equations that describe the propagation of the optical beams through the experimental system are developed, and the signal-processing techniques used to obtain the grating amplitude and phase information are discussed.

#### Signal Creation and Grating Formation

As mentioned in the previous chapter, there are many diffracted orders leaving the MgF<sub>2</sub> grating. Of these, only the +1 and -1 orders satisfy the Bragg condition at Bragg cell #1. Figure 5.1 shows the beam configuration at Bragg cell #1. The fields of these two beams are expressed as

$$\vec{E}_{i1} = \vec{A}(x,y,z)e^{j(\omega_L t - \vec{k}_1 \cdot \vec{r} + \psi_0)}, \quad (5.1)$$

and

$$\vec{E}_{i2} = \vec{B}(x,y,z)e^{j(\omega_L t - \vec{k}_2 \cdot \vec{r})}, \quad (5.2)$$

where  $\vec{k}_1$  and  $\vec{k}_2$  are the incident wave vectors,  $\vec{r}$  is the position vector,  $\vec{A}$  and  $\vec{B}$  are the field amplitudes, and  $\omega_L$  is the optical frequency of the input beams. The phase  $\psi_0$  is the relative shift between the two fields entering the first Bragg cell.

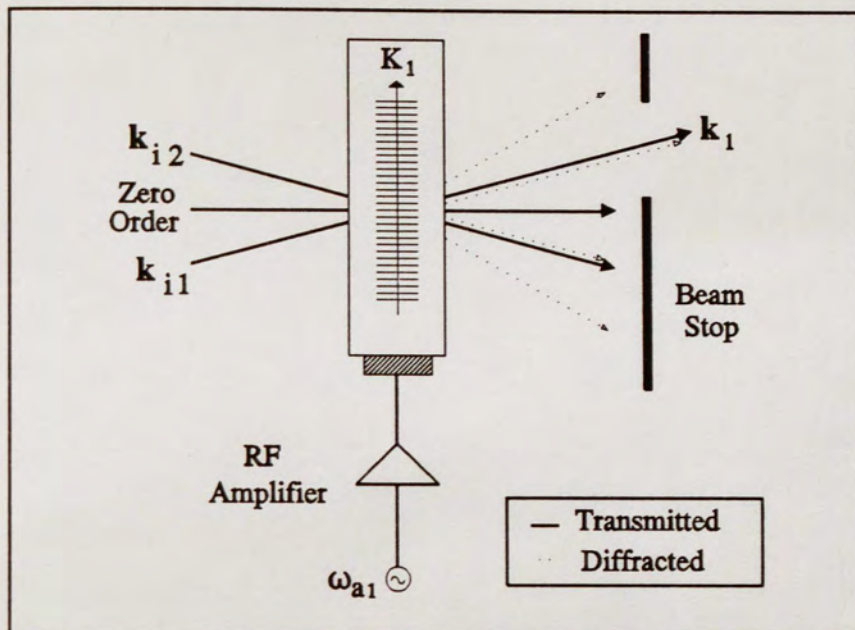


Figure 5.1 Wavevector Diagram for Bragg Cell #1

For notational convenience, several simplifications to equations (5.1) and (5.2) are in order. It was noted in Chapter 4 that the intensities of the +1 and -1 diffracted orders entering the cell were equal to within 1%. Also, the x and y components of the field amplitudes were very small. Therefore, the vector notation for amplitude is dropped and the amplitude of each beam entering Bragg cell #1 is expressed as  $E_o$ , resulting in

$$E_{i1} = E_o e^{j(\omega_L t - \vec{k}_1 \cdot \vec{r} + \psi_o)} \quad E_{i2} = E_o e^{j(\omega_L t - \vec{k}_2 \cdot \vec{r})} \quad (5.3)$$

The acoustic wave  $S$  may be expressed by

$$S \propto \cos(\omega_{a1} t - K_1 z), \quad (5.4)$$

where  $\mathbf{K}_1$  is the acoustic wavevector in the first Bragg cell. The output of the Bragg cell is found by the relation

$$E_{output} = E_{input} \left\{ \cos(\gamma_1) + \sin(\gamma_1) e^{-j\pi/2} \left[ e^{j(\vec{k}_1 \cdot \vec{r} - \omega_{a1}t)} + e^{-j(\vec{k}_1 \cdot \vec{r} - \omega_{a1}t)} \right] \right\}, \quad (5.5)$$

where  $E_{output}$  represents the fields of the two output beams for a given input field  $E_{input}$ . The acoustic grating strength  $\gamma_1$  was identified in equation (2.9). When the Bragg condition is satisfied for both incident beams  $E_{i1}$  and  $E_{i2}$ , the diffracted component of each beam is collinear with the transmitted component of the other. Substituting  $E_{i1}$  and  $E_{i2}$  for  $E_{input}$  in equation (5.5), and applying the phase matching condition  $\mathbf{k}_d = \mathbf{k}_i \pm \mathbf{K}_a$  given in Chapter 2, yields a field expression for  $E_1$ , the beam chosen to continue to the second Bragg cell,

$$E_1 = E_o e^{j\omega_L t} \left\{ \cos(\gamma_1) e^{j(-\vec{k}_1 \cdot \vec{r} + \psi_o)} + \sin(\gamma_1) e^{j\left[\omega_{a1}t - (\vec{k}_1 + \vec{k}_2) \cdot \vec{r} - \frac{\pi}{2}\right]} \right\}, \quad (5.6)$$

where

$$\vec{K}_1 = \vec{k}_1 - \vec{k}_2. \quad (5.7)$$

Note that the frequency of the diffracted component has been shifted up by the driving frequency  $\omega_{a1}$  of the first Bragg cell.

At this point it is appropriate to introduce the dephasing parameter  $\psi_1$ , the phase difference between the diffracted and transmitted components of the field  $E_1$  due to a non-ideal phase matching achieved experimentally. Alignment of the Bragg cell slightly off of the Bragg angle causes a phase shift different from  $-\pi/2$ . One would expect the phase  $\psi_1$  to vary somewhat each time the system is aligned. It is important to track  $\psi_1$  because it is not present at the output of Bragg cell #1 during the read period (RF power off), resulting in a difference between the read and write configurations. Substituting equation (5.7) into the field expression of equation (5.6), and including  $\psi_1$  yields

$$E_1 = E_o e^{j(\omega_L t - \vec{k}_1 \cdot \vec{r})} \left[ \cos(\gamma_1) e^{j\psi_o} + \sin(\gamma_1) e^{j\left(\omega_{a1} t - \frac{\pi}{2} + \psi_1\right)} \right]. \quad (5.8)$$

The intensity  $E_1 E_1^*$  of this beam is

$$I_1 = E_o^2 \left[ 1 + 2 \cos(\gamma_1) \sin(\gamma_1) \sin(\omega_{a1} t - \psi_o + \psi_1) \right]. \quad (5.9)$$

Defining the signal modulation factor  $m$ ,

$$m = \sin(2\gamma_1), \quad (5.10)$$

and assigning  $I_o = E_o^2$  produces an expression used for the intensity of the output of Bragg cell #1,

$$I_1 = I_o \left[ 1 + m \sin(\omega_{a1} t - \psi_o + \psi_1) \right]. \quad (5.11)$$

Thus the goal of the front end of the system, a beam modulated at the driving RF frequency, has been achieved.

The beam of equation (5.8) is directed into the  $\text{TeO}_2$  Bragg cell, Bragg cell #2. The transfer characteristic of this device is modeled by equation (5.5), but with only one input beam. Figure 5.2 shows the beam arrangement at Bragg cell #2. Following the procedure described for the first Bragg cell results in field expressions for the transmitted field  $E_{2T}$  and the diffracted field  $E_{2D}$  of Bragg cell #2,

$$E_{2T} = E_1 \cos(\gamma_2) \quad E_{2D} = E_1 \sin(\gamma_2) e^{j\left(\vec{k}_2 \cdot \vec{r} - \omega_{a2} t - \frac{\pi}{2}\right)}. \quad (5.12)$$



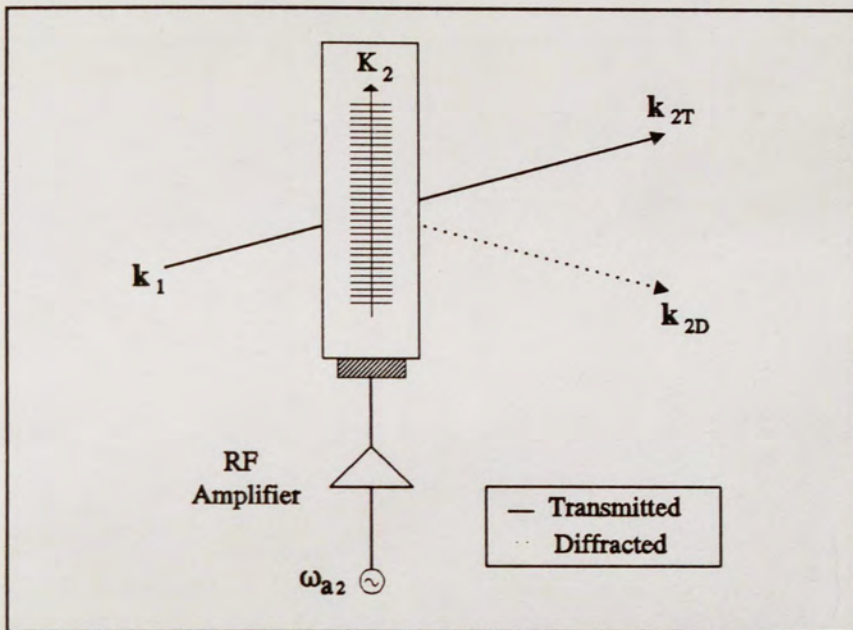


Figure 5.2 Wavevector Diagram for Bragg Cell #2

The notation for the incident wave vector  $\mathbf{k}_1$  is now changed to  $\mathbf{k}_{2T}$  to relate it to Bragg cell #2. This is thought to be more meaningful in later field expressions. The phase matching condition requires that

$$\vec{K}_2 = \vec{k}_{2T} - \vec{k}_{2D}. \quad (5.13)$$

Substituting equation (5.13) into (5.12), and inserting the parameter  $\psi_2$  to account for alignment error at this cell, results in full expressions for the two beams used to build the photorefractive grating,

$$E_{2T} = E_o e^{j(\omega_{a2}t - \vec{k}_{2T} \cdot \vec{r})} \left[ \cos(\gamma_1) \cos(\gamma_2) e^{j\psi_2} + \sin(\gamma_1) \cos(\gamma_2) e^{j(\omega_{a2}t + \psi_1 - \frac{\pi}{2})} \right] \quad (5.14)$$

and

$$E_{2D} = E_o e^{j(\omega_1 t - \vec{k}_{2D} \cdot \vec{r})} \left[ \cos(\gamma_1) \sin(\gamma_2) e^{j(-\omega_{a2} t + \psi_o + \psi_2 - \frac{\pi}{2})} + \sin(\gamma_1) \sin(\gamma_2) e^{j(\psi_1 + \psi_2 - \pi)} \right]. \quad (5.15)$$

$E_{2T}$  and  $E_{2D}$  are forced to overlap in the crystal by the reflection-coated prism and mirrors  $M_1$  and  $M_2$  shown in Figure 4.1, page xx, or by the lens shown in Figure 4.2. The resultant intensity pattern builds the photorefractive grating (Figure 5.3). Accordingly, the intensity at the crystal is given by

$$\begin{aligned} I_c = I_o \{ & 1 + m \sin(\omega_{a1} t - \psi_o + \psi_1) \\ & - \sin(2\gamma_2) \sin[\omega_{a2} t - (\vec{k}_{2T} - \vec{k}_{2D}) \cdot \vec{r} - \psi_2] \\ & - \frac{1}{2} m \sin(2\gamma_2) \cos[(\omega_{a1} - \omega_{a2}) t - (\vec{k}_{2D} - \vec{k}_{2T}) \cdot \vec{r} - \psi_o + \psi_1 + \psi_2] \\ & + \frac{1}{2} m \sin(2\gamma_2) \cos[(\omega_{a1} + \omega_{a2}) t - (\vec{k}_{2D} - \vec{k}_{2T}) \cdot \vec{r} - \psi_o + \psi_1 - \psi_2] \}. \end{aligned} \quad (5.16)$$

It is evident that when  $\omega_{a1} = \omega_{a2}$  the fourth term on the right side of equation (5.16) has spatial dependence only. Since both Bragg cells are driven by the same source, this is always the case. The spatial period is determined by the difference of the wave vectors  $\mathbf{k}_{2D}$  and  $\mathbf{k}_{2T}$ , parameters which are controlled experimentally. The spatially-modulated intensity pattern excites charge carriers as described in Chapter 3. Note that the phase of the intensity pattern for the condition  $\omega_{a1} = \omega_{a2}$  contains the phase difference  $\psi_o$  of the two beams incident on Bragg cell #1, as well as the dephasing parameters  $\psi_1$  and  $\psi_2$ . Since this spatial light pattern induces grating formation, all three phase terms are written into the holographic grating. In the discussion of Chapter 3 it was stated that, in general, there exists a shift between the grating phase and the intensity pattern. This grating shift  $\phi$  is now added to the term in

equation (5.16) for the condition  $\omega_{a1} = \omega_{a2}$ . For convenience in subsequent equations the resultant absolute grating phase is labeled  $\phi'$ ,

$$\phi'(t) = \psi_0 - \psi_1 - \psi_2 - \phi(t) + \pi. \quad (5.17)$$

### Field Analysis at the Detector

The discussion of the last few pages has shown field equations for the heterodyne signal leaving Bragg cell #1, and how the two beams from Bragg cell #2 combine within the photorefractive crystal to induce a grating. The next step in the signal development is inclusion the effect of the photorefractive grating on the signal as it passes through the crystal and arrive at an expression for the intensity of the beams leaving the crystal.

As in the case of an acoustic grating, a beam incident on a photorefractive grating is divided into transmitted and diffracted beams. Unlike the acoustic gratings, there is no Doppler shift because the photorefractive grating is stationary. Equation (5.5) can be used once more to describe the input-output relation of the fields by setting the acoustic frequency to zero. The fields incident on the crystal (Figure 5.3) are  $E_{2T}$  and  $E_{2D}$ , equation (5.15). The fields of the output beams  $E_A$  and  $E_B$  are given by

$$E_A(t) = E_1 \left\{ \cos(\gamma_2) \cos[\gamma_c(t)] + \sin(\gamma_2) \sin[\gamma_c(t)] e^{j[(\vec{k}_2 - \vec{k}_c) \cdot \vec{r} - \omega_a t + \psi_2 + \phi'(t) - \pi]} \right\}, \quad (5.18)$$

and

$$E_B(t) = E_1 \left[ \sin(\gamma_2) \cos[\gamma_c(t)] e^{j\left(\vec{k}_2 \cdot \vec{r} - \omega_{a2} t + \psi_2 - \frac{\pi}{2}\right)} + \cos(\gamma_2) \sin[\gamma_c(t)] e^{j\left(\vec{k}_c \cdot \vec{r} - \phi'(t) - \frac{\pi}{2}\right)} \right], \quad (5.19)$$

where the grating vector in the crystal,  $\vec{K}_c$ , is defined by

$$\vec{K}_c = (\vec{k}_{2T} - \vec{k}_{2D}), \quad (5.20)$$

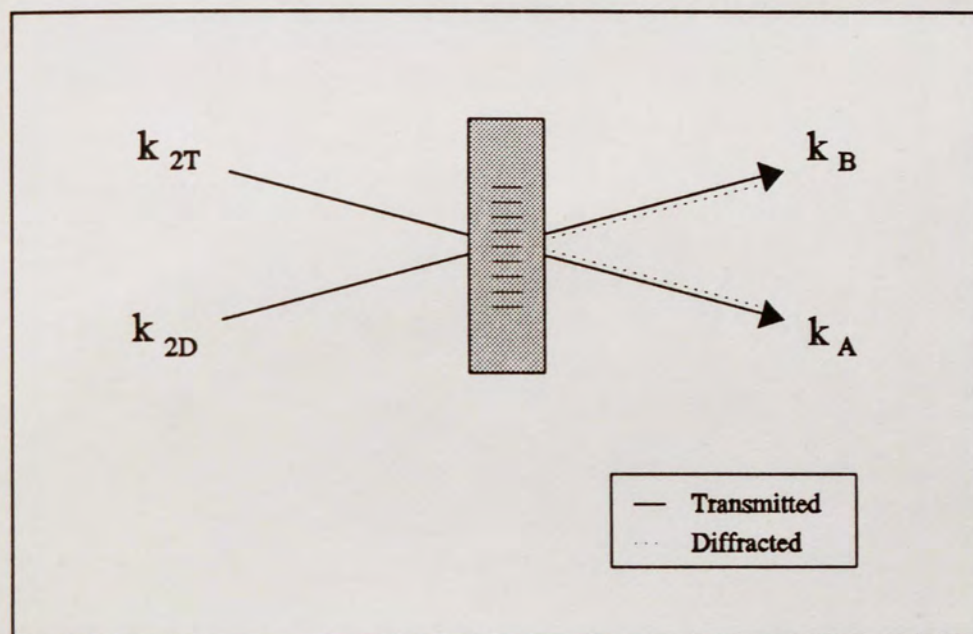


Figure 5.3 Wavevector Diagram for the Photorefractive Crystal

The grating strength  $\gamma_c$  of the holographic grating is given by [30]

$$\gamma_c(t) = \frac{\pi d \Delta n(t)}{\lambda}. \quad (5.21)$$

Recall that  $d$  is the interaction length and  $\Delta n$ , defined in equation (3.7), is the change of refractive index induced by the space charge field. Note that as the two beams  $E_{2T}$  and  $E_{2D}$  passed through the crystal the phase  $\phi'$  was incorporated into the field expression. This is a dynamic phenomenon. The presence of the photorefractive grating changes the configuration of the write beam as the grating builds.

The beams are now in position to be processed by the electronics. Accordingly, the intensities must be calculated in order to find the response of the detector. Using equation (5.20) and the performing the operation  $E_A E_A^*$  gives an expression for the beam with wavevector  $k_a$ ,

$$\begin{aligned}
 I_a(t) = I_o \{ & P_1(t) + m P_1(t) \sin(\omega_{a1} t - \psi_o + \psi_1) \\
 & - \frac{1}{2} \sin(2\gamma_2) \sin[2\gamma_c(t)] \cos[\omega_{a2} t - \psi_o + \psi_1 + \phi(t)] \\
 & - \frac{1}{4} m \sin(2\gamma_2) \sin[2\gamma_c(t)] \cos[(\omega_{a1} + \omega_{a2})t - 2\psi_o + 2\psi_1 + \phi(t)] \\
 & + \frac{1}{4} m \sin(2\gamma_2) \sin[2\gamma_c(t)] \cos[(\omega_{a1} - \omega_{a2})t - \phi(t)] \}.
 \end{aligned} \tag{5.22}$$

where

$$P_1(t) = \sin^2(\gamma_2) \sin^2[\gamma_c(t)] + \cos^2(\gamma_2) \cos^2[\gamma_c(t)]. \tag{5.23}$$

The intensity for beam  $E_B$  is expressed by

$$\begin{aligned}
 I_B(t) = I_o \{ & P_2(t) + m P_2(t) \sin(\omega_{a1} t - \psi_o + \psi_1) \\
 & + \frac{1}{2} \sin(2\gamma_2) \sin[2\gamma_c(t)] \cos[\omega_{a2} t - \psi_o + \psi_1 + \phi(t)] \\
 & + \frac{1}{4} m \sin(2\gamma_2) \sin[2\gamma_c(t)] \cos[(\omega_{a1} + \omega_{a2})t - 2\psi_o + 2\psi_1 + \phi(t)] \\
 & - \frac{1}{4} m \sin(2\gamma_2) \sin[2\gamma_c(t)] \cos[(\omega_{a1} - \omega_{a2})t - \phi(t)] \},
 \end{aligned} \tag{5.24}$$

where

$$P_2(t) = \cos^2(\gamma_2) \sin^2[\gamma_c(t)] + \sin^2(\gamma_2) \cos^2[\gamma_c(t)]. \tag{5.25}$$

Equations (5.22) and (5.24) describe the intensity of the two first-order beams leaving the photorefractive crystal. From the field analysis of the previous section it is clear that the system does not lack symmetry. Both of the first-order beams contain identical information regarding the grating. In the experiment, the detector was placed in the path of the beam with wavevector  $\mathbf{k}_a$  for convenience. Also, in the field analysis the angular frequencies of the signals driving the Bragg cells were labeled  $\omega_{a1}$  and  $\omega_{a2}$  in order to show the interaction of the two A-O cells. In the experiment, the Bragg cells were driven by the same RF source and the condition  $\omega_{a1} = \omega_{a2}$  was always true. Henceforth, the notation will be simplified to  $\omega_a$ .

The network analyzer continuously compares the signal from the detector to the reference signal. Since the network analyzer is tuned to the driving frequency, it only detects those components of the intensity defined in equation (5.22) that are within 5 kHz of  $\omega_a$ . The signal experiences an unknown gain as it is processed by the electronics. Accordingly, the signal seen by the network analyzer during the write period ( $m \approx 1$ ) is given by

$$\begin{aligned}
 S_w(t) &\propto I_o \left\{ m P_1(t) \sin(\omega_{a1} t - \psi_o + \psi_1) \right. \\
 &\quad \left. - \frac{1}{2} \sin(2\gamma_2) \sin[2\gamma_c(t)] \cos[\omega_{a2} t - \psi_o + \psi_1 + \phi(t)] \right\} \quad (5.26) \\
 &\equiv A(t) \sin(\omega_a t - \psi_o + \psi_1) + B(t) \sin[\omega_a t + \theta(t)],
 \end{aligned}$$

where  $P_1(t)$  was defined in Eq. (5.23) and

$$A(t) = c m P_1(t), \quad (5.27)$$

$$B(t) = \frac{1}{2} c \sin(2\gamma_2) \sin[2\gamma_c(t)], \quad (5.28)$$

and

$$\theta(t) = -\psi_o + \psi_1 + \phi(t) - \frac{\pi}{2}. \quad (5.29)$$

The constant  $c$  includes a gain factor due to the electronic processing. It is clear that the separation of the two terms of equation (5.26) will result in increased sensitivity in the monitoring of the grating. For the read cycle the RF power to the first Bragg cell is interrupted briefly to read the grating. The signal seen by the network analyzer during the read cycle ( $m=0$ ) is given by

$$\begin{aligned} S_R(t) &\propto -\frac{1}{2} I_o \sin(2\gamma_2) \sin[2\gamma_c(t)] \cos[\omega_{a2}t - \psi_o + \psi_1 + \phi(t)] \\ &\equiv B(t) \sin[\omega_a t + \theta(t)]. \end{aligned} \quad (5.30)$$

A needed reference for amplitude and phase is provided by equation (5.26) at time  $t=0$ , immediately after the modulation has been turned on for the first time. At time  $t=0$ ,  $B(t)=0$  because there is no grating present ( $\gamma_c=0$ ). Also,  $P_1(t)$ , defined in equation (5.23), reduces to  $P_1(t=0) = \cos^2(\gamma_2)$ . For amplitude, subtraction of the write amplitude, equation (5.26), at time  $t=0$  from the read amplitude, equation (5.35), results in

$$B(t) - A(t=0) = 20 \log \left\{ \frac{\tan(\gamma_2)}{m} \sin[2\gamma_c(t)] \right\}. \quad (5.31)$$

Recall that the network analyzer reports amplitude data on a log scale. Inserting  $\gamma_c$ , the photorefractive grating strength defined in equation (5.21), and  $\Delta n$ , given in equation (3.7),

page 11, results in an expression relating the amplitude of the space-charge field to the measured data,

$$E_{sc}(t) = \frac{\lambda}{\pi d n_e^3 r_{33}} \sin^{-1} \left[ \frac{m}{\tan(\gamma_2)} 10^{\frac{B(t) - A(t=0)}{20}} \right]. \quad (5.32)$$

For the photorefractive phase  $\phi$ , subtraction of the write expression at time  $t=0$  from the read expression gives

$$\phi(t) = \theta(t) + \psi_o - \psi_1 + \frac{\pi}{2}. \quad (5.33)$$

It can be seen that isolation and calculation of the amplitude and phase of the space-charge field from the measured data is direct and straightforward. It is clear that the unknown phase components  $\psi_o$ ,  $\psi_1$ , and  $\psi_2$  have been negated by the memory of the photorefractive grating, leaving only the photorefractive phase  $\phi$ . In this sense the system is self-correcting.

In summary, it has been shown that the configuration of Bragg cells and beam-steering equipment produces a stationary, sinusoidal intensity pattern at the crystal to induce grating formation. The unknown phase shift  $\psi_o$  between the two beams entering the first Bragg cell and the dephasing parameters  $\psi_1$  and  $\psi_2$  are stored in the holographic grating. Portions of the recording beams are diffracted by the grating as they pass through the crystal, acquiring the phase components  $\psi_o$ ,  $\psi_1$ ,  $\psi_2$ , and the photorefractive phase component  $\phi$  in the diffraction process. The presence of a photorefractive grating manifests as an intensity-modulated component of the beam that illuminates the photodetector. The electronically controlled write-read cycles provide a simple means of separating the amplitude and phase of the space-charge field from the composite signal present during the recording of the grating. This information is observable on the network analyzer display as the the experiment is performed.



## CHAPTER 6

### EXPERIMENT

This chapter relates some of the techniques employed in data acquisition and interpretation of the data. A sample graph of raw measured data is used to illustrate some of the features of the measurement technique. Experimental results are shown as a function of spatial frequency for the  $\text{KNbO}_3\text{:Fe}$ ,  $\text{KNbO}_3\text{:Ta}$ ,  $\text{BaTiO}_3$ , and  $\text{LiNbO}_3\text{:Fe}$  crystals. A more in-depth analysis of the data appears in the next chapter.

#### Testing

Experimental runs for each crystal were made in pairs, with the crystals rotated  $180^\circ$  between runs so the c-axis pointed in opposite directions. The actual direction of the optic axis is known only for  $\text{LiNbO}_3\text{:Fe}$ . Measurements were taken at three grating spacings for each crystal:  $\Lambda = 1.5 \mu\text{m}$ ,  $\Lambda = 2.5 \mu\text{m}$ , and  $\Lambda = 10.5 \mu\text{m}$ . The beam diameter at the crystal was about 3.5 mm, giving an intensity of about  $100 \text{ mW/cm}^2$ . The configuration of Figure 4.1 was used for the 1.5 and 2.5  $\mu\text{m}$  spacings, and the configuration of Figure 4.2 was used for the 10.5  $\mu\text{m}$  spacing. The configuration of Figure 4.2 was the initial system configuration.

Experimental runs began with the shutter closed and the crystal in the dark. Several data points were taken in order to establish a dark noise floor for both amplitude and phase. Ideally, the phase reported during this time was random.

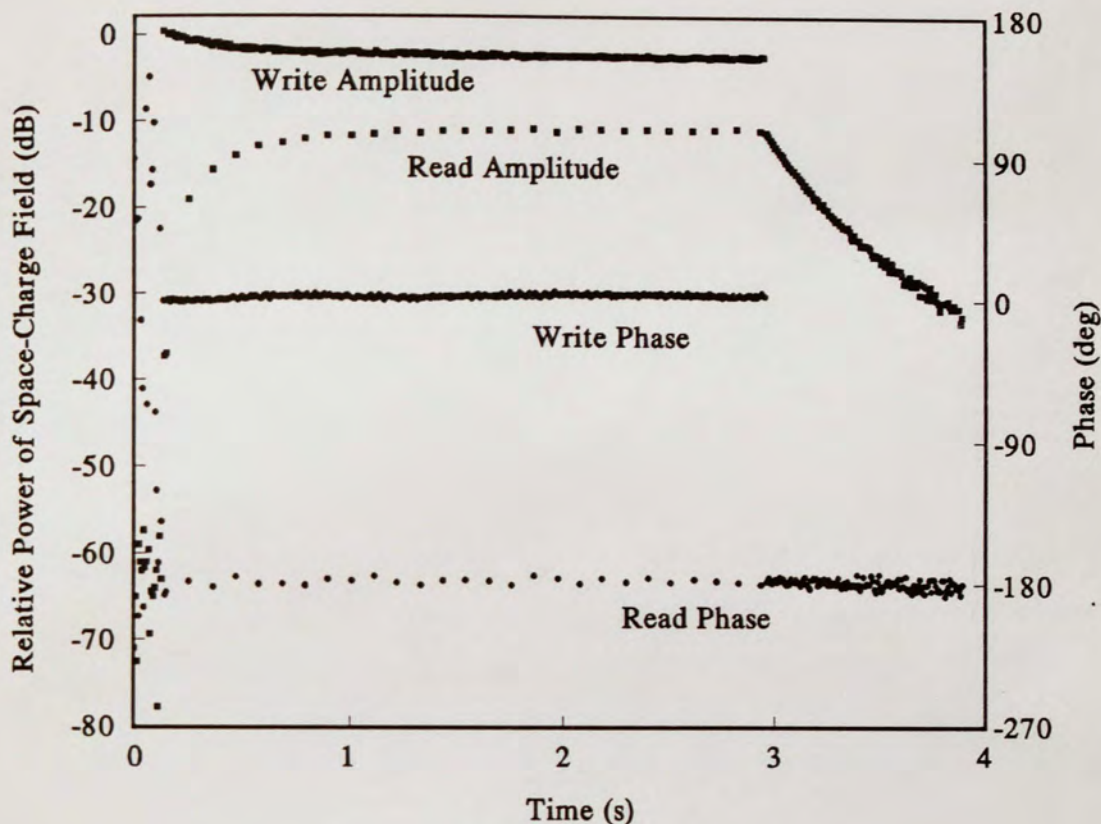


**Figure 6.1**  
 Measured Amplitude and Phase Data  
 $\text{KNbO}_3:\text{Ta}$ ,  $I = 100 \text{ mW/cm}^2$ ,  $\Lambda = 2.5 \mu\text{m}$

These measurements determined whether an unwanted RF signal was infiltrating the electronics. The shutter was then opened, illuminating the crystal, and noise measurements were taken with RF power to the first Bragg cell off ( $m=0$ ). A jump in the amplitude curve coupled with stable phase readings at this point would indicate that an undesired signal was present on the read beam. Minimization of the signal during the noise measurements was important for several reasons. First, a low amplitude noise floor gives a high dynamic range for the grating amplitude signal, enabling measurement of crystal fields at the very beginning of grating formation. Second, random phase readings during the noise measurement period indicate that there was no coherent signal for the network analyzer to lock on to, and the first

stable phase point during grating formation can be attributed to the grating. If there was a signal present during the noise measurements, it must be taken into account when interpreting the first few read points of the grating. Therefore, RF shielding and the input-output isolation of the RF switches controlling power to the first Bragg cell were of primary concern. Figure 6.1, measured data from an experimental run with  $\text{KNbO}_3:\text{Ta}$ , shows a noise floor varying from about 60 to 70 dB below the write amplitude, and random phase during the noise measurements. Figure 6.1 is an example of a clean data run, i.e. there was no coherent signal present during the noise measurements. Following the noise measurements, power to Bragg cell #1 was turned on for the initial write period, and the write-read cycles continued until the grating had saturated. The actual write and read times varied for each crystal, and, typically, a read period lasted from 4% to 7% of the time taken for a write period. At least three amplitude and three phase measurements were made during each read period, and the read time was kept as small as possible to avoid significant erasure of the grating. Notice, in Figure 6.1, that the amplitude of the write signal decayed as the grating built, and then flattened out as the grating reached saturation. For this data run, the phase difference between the write and read signals was about  $180^\circ$ . Equation (5.26), page 37, shows that, as  $\gamma_c$  increased, the effect of the grating on the write signal became more pronounced. Since the phase of the two components were in opposition for this run, the decay of the composite write signal can be expected. Remember that the phase difference between read and write signals depends on the grating phase. After the grating had saturated, the modulation was permanently turned off for measurement of the grating decay.

The readings for each period were averaged, and equations (5.32) and (5.33) were applied to the amplitude and phase data, respectively.

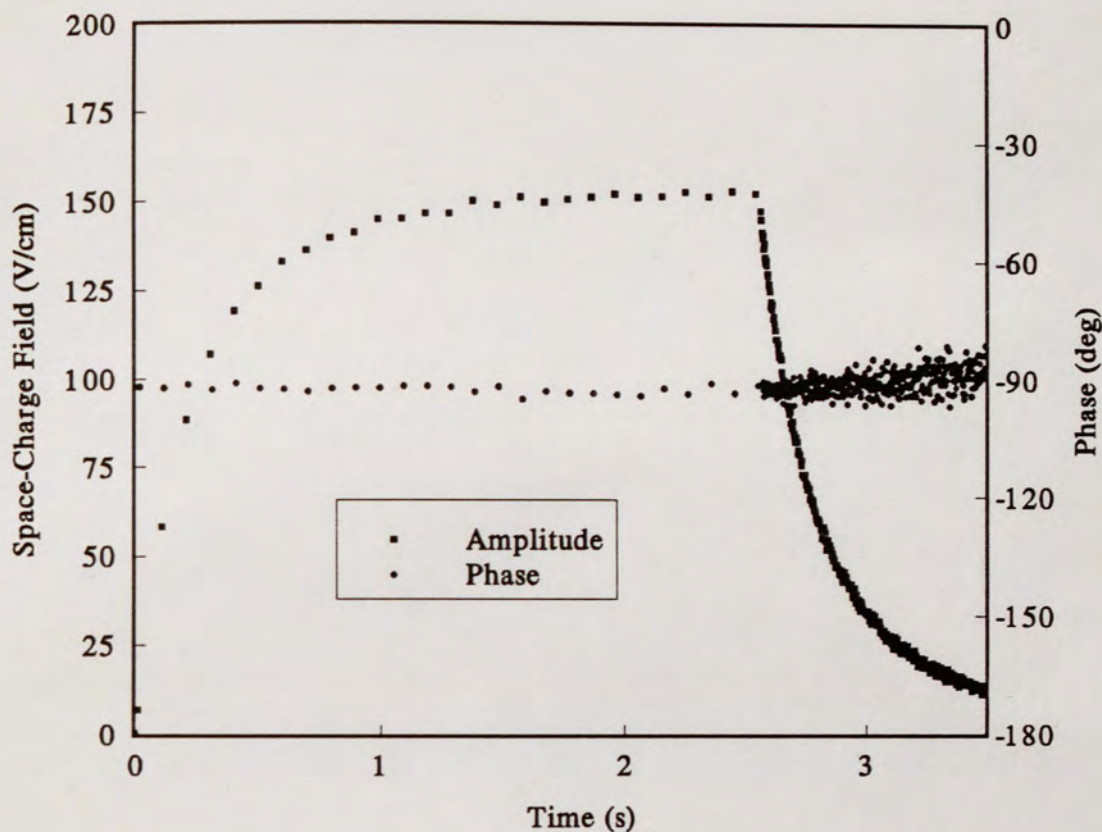


**Figure 6.2**  
Amplitude and Phase of the Space-Charge Field  
from the data of Figure 6.1

Because the grating development was interrupted during the read cycle, the read time for each read period was subtracted from the time axis in order to arrive at a more accurate time dependence of the crystal response. Figure 6.2 shows the result of these operations for the measured data of Figure 6.1. It is interesting to note the increasing phase instability as the grating amplitude decayed, underlining the importance of the signal to noise ratio. Also, the first measured amplitude point is about 5 V/cm, corresponding to a  $\Delta n$  of about  $2.5 \times 10^{-7}$  for  $\text{KNbO}_3:\text{Ta}$ . Table 6.1, below, lists the electro-optic coefficients, the grating thicknesses  $d$ , extraordinary refractive indices, and the A.C. relative permittivities used in calculations for

the four crystals. The absorption coefficients  $\alpha$  were measured for each crystal in a separate experiment.

TABLE 6.1  
PARAMETERS FOR THE PHOTOREFRACTIVE CRYSTALS

CRYSTAL	d (mm)	$r_{33}$ ( $10^{-12}\text{m/V}$ )	$n_e$	$\epsilon_r$	$\alpha$ ( $\text{cm}^{-1}$ )
BaTiO <sub>3</sub>	2.7	105 <sup>[5]</sup>	2.365 <sup>[11]</sup>	135 <sup>[18]</sup>	1.06
KNbO <sub>3</sub> :Ta	5.0	64 <sup>[11]</sup>	2.169 <sup>[11]</sup>	55 <sup>[5]</sup>	.158
KNbO <sub>3</sub> :Fe	5.0	64 <sup>[11]</sup>	2.169 <sup>[11]</sup>	55 <sup>[5],a</sup>	.274
LiNbO <sub>3</sub> :Fe	5.0	30.9 <sup>[11]</sup>	2.200 <sup>[11]</sup>	-- <sup>a</sup>	1.09

<sup>a</sup> Not used

### Experimental Results for BaTiO<sub>3</sub>

A total of 26 experimental runs were taken for BaTiO<sub>3</sub>: 18 runs at  $\Lambda = 10.5 \mu\text{m}$ , and 4 each at the 1.5 and 2.5  $\mu\text{m}$  spacings. Figure 6.3 shows the photorefractive response of BaTiO<sub>3</sub> as a function of spatial frequency. The amplitude and phase data were processed as outlined above for the data of Figure 6.2. The solid lines are least-squares fits for the time dependence of the amplitude of the space-charge fields given in equation (3.29), page 18, with the effective time constant  $\tau_{\text{eff}}$  as the unknown variable. The results for BaTiO<sub>3</sub> were very clean and consistent at 1.5 and 2.5  $\mu\text{m}$ , while the 10.5  $\mu\text{m}$  data showed more variation from run to run.

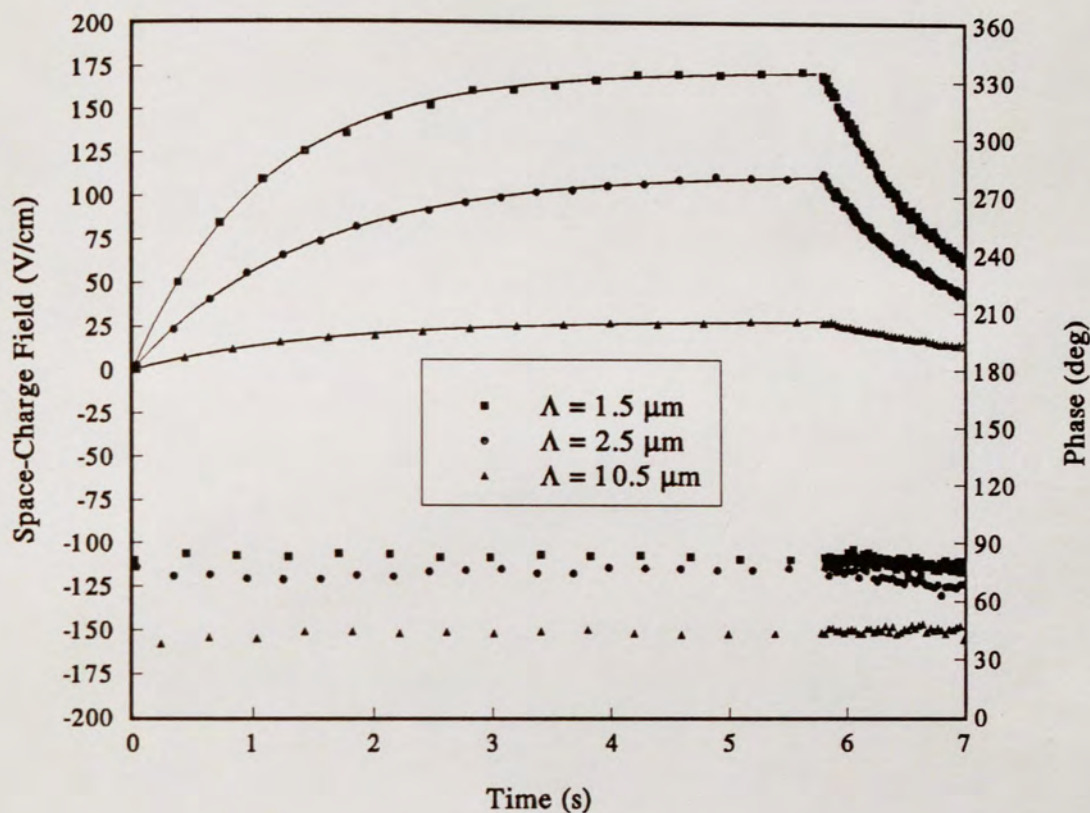


**Figure 6.3**  
Amplitude and Phase of the Space-Charge Fields in  $\text{BaTiO}_3$   
as a Function of Spatial Frequency

The field phase was different from  $90^\circ$  for each spatial frequency. Recall from the photorefractive field equations that this indicates the presence of a photovoltaic field in  $\text{BaTiO}_3$ . The fact that the phase moved toward  $90^\circ$  as the spatial frequency increased is indicative that the diffusion field became more dominant at higher spatial frequencies. Table 6.2 shows averaged numbers for the saturation values of the diffraction efficiency  $\eta = \sin^2(\gamma_c)$ ,  $\Delta n$ , the saturation amplitude of the space-charge field, the effective time constant  $\tau_{\text{eff}}$ , and the phase of the space-charge field  $\phi$  at saturation for the three spatial frequencies. All of these

parameters were calculated directly from the measured data with reference to the material constants listed in Table 6.1 when necessary.

TABLE 6.2  
MEASURED FIELD PARAMETERS FOR BaTiO<sub>3</sub>

$\Lambda$ ( $\mu\text{m}$ )	$\Delta n$ ( $\times 10^{-6}$ )	$E_{\text{sc}}$ (V/cm)	$\Delta E_{\text{sc}}$ (%)	$\eta$ (%)	$\phi$ (deg)	$\Delta\phi$ ( $\pm$ deg)	$\tau_{\text{eff}}$ (s)	$\Delta\tau_{\text{eff}}$ (%)
1.5	12	172	12	3.8	84	3	1.1	10
2.5	8.4	122	10	1.9	75	7	1.4	10
10.5	1.6	23	25	.07	40	15	1.9	20

$\Delta E_{\text{sc}}$  and  $\Delta\tau_{\text{eff}}$  refer to the maximum percentage of variation about the average for all runs at the grating period listed, and  $\Delta\phi$  refers to the maximum variation in the saturation phase. The numbers in the table reflect the averages for both crystal orientations. There was no significant difference in the grating amplitudes and time constants with respect to the two orientations. The phase readings for one orientation were all negative for this crystal, and those for the opposite direction were all positive. This indicates a change of sign in the diffusion field as the c-axis was rotated. For simplicity, the absolute values of the phase readings were taken before averaging for the table. The only difference in the absolute values of the phase readings for the two orientations, including all crystals and all spatial frequencies, was in the 10.5  $\mu\text{m}$  data for BaTiO<sub>3</sub>, where the where a 6° difference existed. This is not considered significant

for the following reasons. First, the spread in phase data for this spatial frequency was more than desirable, perhaps due to the relatively weak fields at the  $10.5 \mu\text{m}$ . Second, alignment of the crystal exactly normal to the bisector of the two laser beams was difficult at  $10.5 \mu\text{m}$ . Non-normal alignment would add an additional phase term to the grating phase not accounted for in the modeling equations presented in Chapter 5. Third, inspection of equation (3.28), page 17, and equations (3.20) and (3.21), page 15, shows that any asymmetry with respect to the orientation of the c-axis is due to  $E_D'$ . The first term in  $E_D'$  is attributable to diffusion and changes sign with axis rotation. The second term is due to the photovoltaic effect and has no dependence on the c-axis orientation. Since both terms are proportional to  $K$ , the asymmetry should be visible at all spatial frequencies. A difference was not visible at the higher spatial frequencies, where it was possible to align the crystal more precisely. It is evident that consistency improved with increased spatial frequency.

The theoretical amplitude curves agreed closely with the measured data for virtually every run. Although there was up to a 20% variation in the time constants calculated at  $10.5 \mu\text{m}$ , the fits modeled the time dependence of individual runs very well at all spatial frequencies. Figure 6.4 shows  $\Delta n$ , which is proportional to the space-charge field, and the diffraction efficiency,  $\eta$ , calculated from the theoretical  $1.5 \mu\text{m}$  amplitude curve of Figure 6.3.



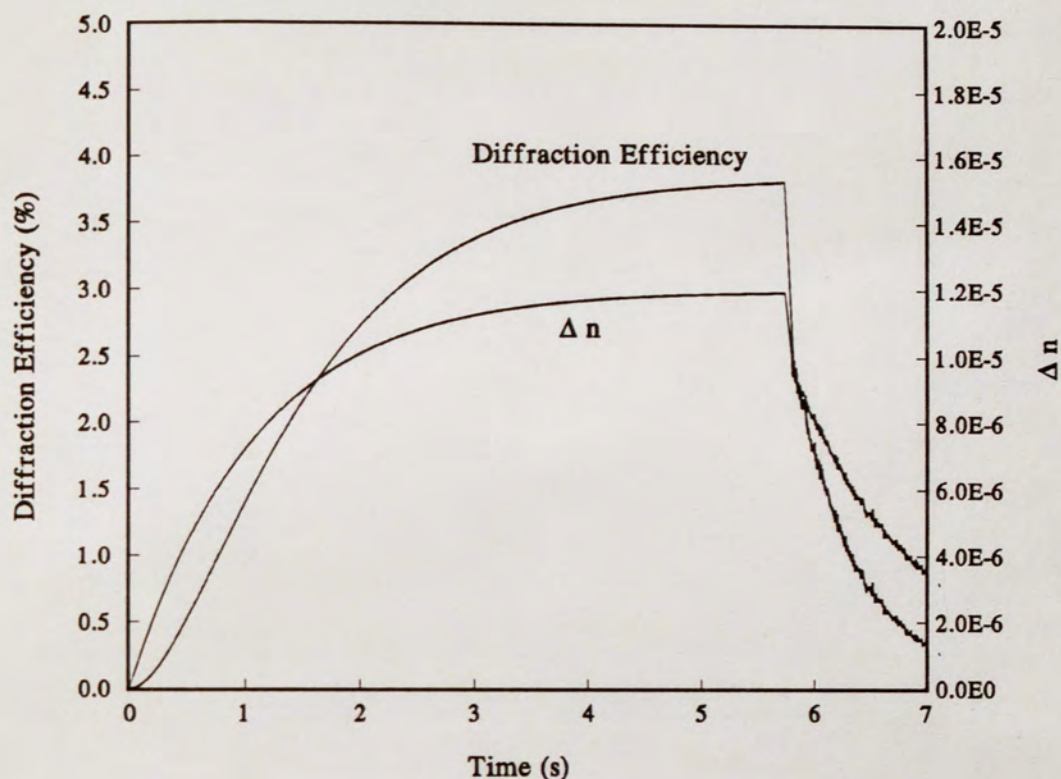


**Figure 6.4**  
Diffraction Efficiency and  $\Delta n$  in  $\text{BaTiO}_3$ ,  $\Lambda = 1.5 \mu\text{m}$

Material properties calculated from the grating parameters shown here will be presented in the next chapter.

### Experimental Results for $\text{KNbO}_3:\text{Ta}$

The tantalum-doped potassium niobate crystal displayed the most consistent results of the four crystals investigated in both amplitude and phase. Seventeen runs were made for  $\text{KNbO}_3:\text{Ta}$  at  $10.5 \mu\text{m}$ , four at  $2.5 \mu\text{m}$ , and six at  $1.5 \mu\text{m}$ . Figure 6.5 shows examples of the response of  $\text{KNbO}_3:\text{Ta}$  as a function of spatial frequency. The solid curves are theoretical amplitude fits.

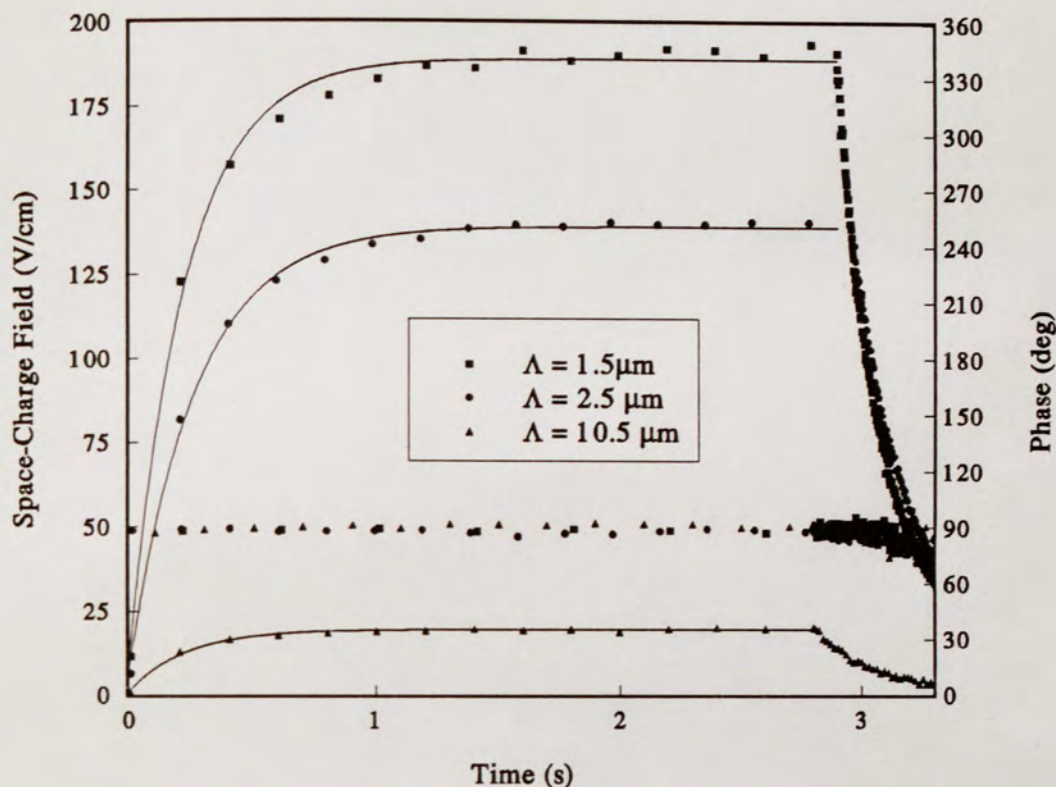


**Figure 6.5**  
Amplitude and Phase of the Space-Charge Fields in  $\text{KNbO}_3:\text{Ta}$   
as a Function of Spatial Frequency

As with  $\text{BaTiO}_3$ , the spatial dependence of the amplitude is clear. The phase of the fields in  $\text{KNbO}_3:\text{Ta}$  was very close to  $90^\circ$  for all three spatial frequencies, indicating that there was little or no photovoltaic field in this crystal. The deviation of the theoretical fits from the measured amplitudes at the knee of the curves seen in the figure was fairly consistent. The cause of this deviation has not been identified. In reference [8], a model is given that allows for two independent sets of photoactive carriers. The dominant carriers are holes for one trap site and electrons for the other. Unlike the single valence-pair model used in this analysis, the effect of two carriers can not be combined into an effective time constant. This is an interesting concept, but requires a more thorough characterization of the crystal response as

a function of spatial frequency. Also note that the response of  $\text{KNbO}_3:\text{Ta}$  is much faster than that of  $\text{BaTiO}_3$ , a desirable property for many signal-processing applications. A table of measured grating parameters is shown below. Again, absolute values of the phase are shown in the table.

TABLE 6.3  
MEASURED FIELD PARAMETERS FOR  $\text{KNbO}_3:\text{Ta}$

$\Lambda$ ( $\mu\text{m}$ )	$\Delta n$ ( $\times 10^{-6}$ )	$E_{\text{sc}}$ (V/cm)	$\Delta E_{\text{sc}}$ (%)	$\eta$ (%)	$\phi$ (deg)	$\Delta\phi$ ( $\pm$ deg)	$\tau_{\text{eff}}$ (s)	$\Delta\tau_{\text{eff}}$ (%)
1.5	6.1	188	6	3.5	90	3	.23	10
2.5	4.7	144	6	2.1	89	4	.26	10
10.5	.73	21	25	.05	86	15	.29	20

It is clear that the crystal response was less consistent at 10.5  $\mu\text{m}$  than at the smaller grating periods. This trend was visible in the data for all crystals. A more detailed analysis of the data for  $\text{KNbO}_3:\text{Ta}$  will be seen in Chapter 6.

#### Experimental Results for $\text{LiNbO}_3:\text{Fe}$

Due to the long storage time of  $\text{LiNbO}_3:\text{Fe}$  it was necessary to handle it differently from the other crystals. After exposure of a selected area of the crystal for a data run, the crystal was translated so that the next run illuminated a different part of the crystal. After several runs, the  $\text{LiNbO}_3:\text{Fe}$  crystal was placed into an oven and heated at about 175° celsius

for 30 minutes or so to erase the recorded gratings. It was then allowed to cool for several hours before further experimentation. There were 20 experimental runs taken with  $\text{LiNbO}_3:\text{Fe}$ : 12 at  $10.5 \mu\text{m}$ , and 4 each at  $1.5$  and  $2.5 \mu\text{m}$ .  $\text{LiNbO}_3:\text{Fe}$  displayed the highest diffraction efficiency of the four crystals, and a correspondingly long saturation time. Sample data showing the photorefractive response of  $\text{LiNbO}_3:\text{Fe}$  appear in Figure 6.6.

The time dependence for  $\text{LiNbO}_3:\text{Fe}$  was different from the other crystals in several respects. First, the amplitude actually decreased after reaching a

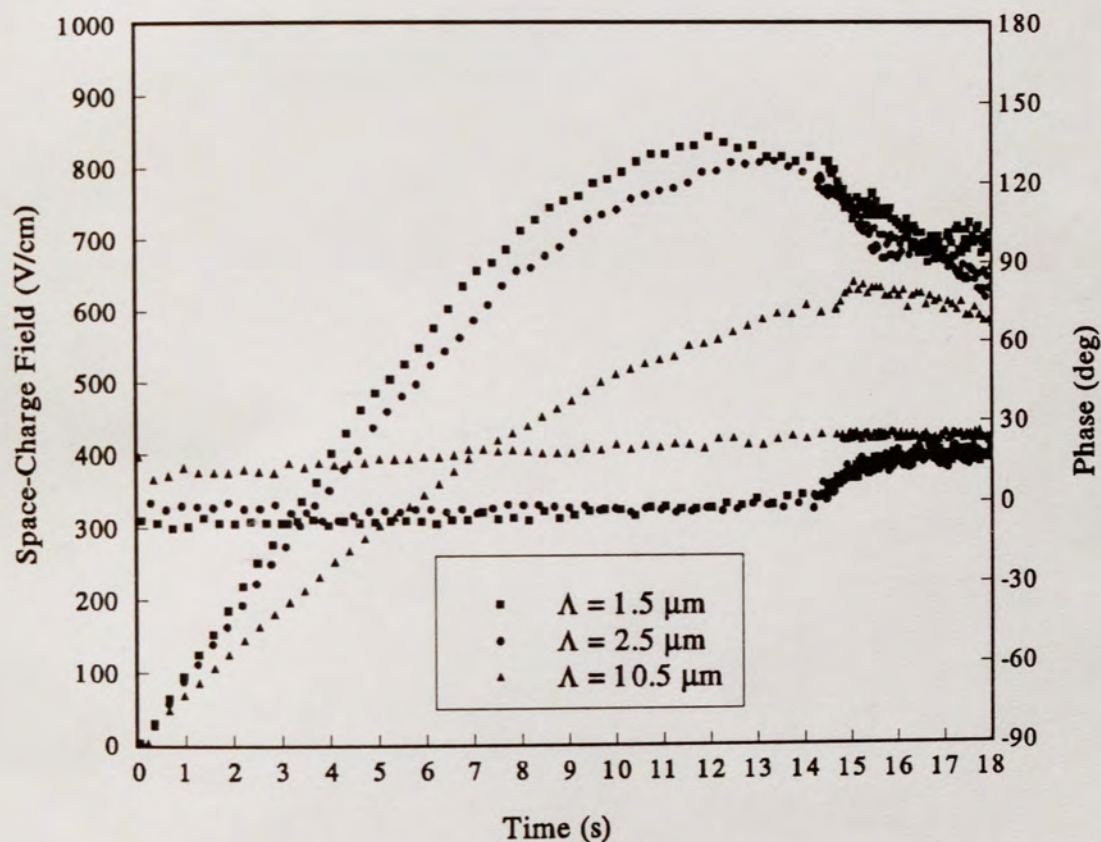


**Figure 6.6**  
Amplitude and Phase of the Space-Charge Fields in  $\text{LiNbO}_3:\text{Fe}$   
as a Function of Spatial Frequency

maximum in many of the runs. It is thought that excessive scattering, a documented phenomenon in  $\text{LiNbO}_3:\text{Fe}$ , may have caused this retardation of the amplitude. In other runs of the same exposure time, it was clear that the grating never saturated. Second, the exponential model for the time dependence does not fit the data for  $\text{LiNbO}_3:\text{Fe}$ . It can be seen in the figure that the slopes of the amplitude curves are approximately linear for a great deal of the exposures. In an attempt to understand the time dependence, numerical experimentation was conducted, in which a time constant was calculated using only the first half or so of the amplitude curves, before the retardation effects were visible. Given the solved time constant, the saturation amplitude was extrapolated to estimate the saturation field in the absence of scattering. The results of this experimentation predict saturation fields of over 3 kV/cm for many runs, and over 5 kV/cm for some. Clearly, these are not physically realistic numbers, since a 100% diffraction efficiency grating in  $\text{LiNbO}_3:\text{Fe}$  would correspond to about 3 kV/cm. Therefore, calculation of time constants for  $\text{LiNbO}_3:\text{Fe}$  was not possible. The phase of  $\text{LiNbO}_3:\text{Fe}$  was usually close to  $0^\circ$ , indicating a strong photovoltaic field. As with the other crystals, the data at  $10.5 \mu\text{m}$  were the least consistent of the three grating periods. The measured data for  $\text{LiNbO}_3:\text{Fe}$  are summarized in the table below.

The sign of the saturation phase for  $\text{LiNbO}_3:\text{Fe}$  showed no dependence on the crystal orientation. Because of the anisotropy of the photovoltaic current, rotation the crystal not only changes the sign of  $\Delta n$  but the direction of the photovoltaic current also, canceling the sign change. A small trend in the phase is visible as a function of spatial frequency, and this trend is opposite to that of  $\text{BaTiO}_3$ . The models predict no such behavior.

TABLE 6.4  
MEASURED FIELD PARAMETERS FOR  $\text{LiNbO}_3:\text{Fe}$

$\Lambda$ ( $\mu\text{m}$ )	$\Delta n$ ( $\times 10^{-6}$ )	$E_{sc}$ (V/cm)	$\Delta E_{sc}$ (%)	$\eta$ (%)	$\phi$ (deg)	$\Delta\phi$ ( $\pm$ deg)
1.5	14	872	8	18	0	3
2.5	14	862	10	18	4	4
10.5	14	853	45	18	10	27

A disappointing amount of quantitative information was gained from the data for  $\text{LiNbO}_3:\text{Fe}$ . The method of data analysis outlined in the next chapter proved to be fruitless for  $\text{LiNbO}_3:\text{Fe}$ . Other than the observations made here, the data has yielded little information. It is thought that inhomogeneous doping may have contributed to the inconsistency of the data for  $\text{LiNbO}_3:\text{Fe}$ .

#### Experimental Results for $\text{KNbO}_3:\text{Fe}$

$\text{KNbO}_3:\text{Fe}$  was the least interesting of the four crystals, displaying lethargic response at all spatial frequencies. There were 20 data runs taken with  $\text{KNbO}_3:\text{Fe}$ : 14 at 10.5  $\mu\text{m}$ , and 4 each at 1.5 and 2.5  $\mu\text{m}$ . Other than displaying the experimental results, very little will be said about  $\text{KNbO}_3:\text{Fe}$ . There are defects within the crystal visible to the naked eye. It is thought that this crystal was very poorly poled. Representative curves for the measured data appear in the graph below.

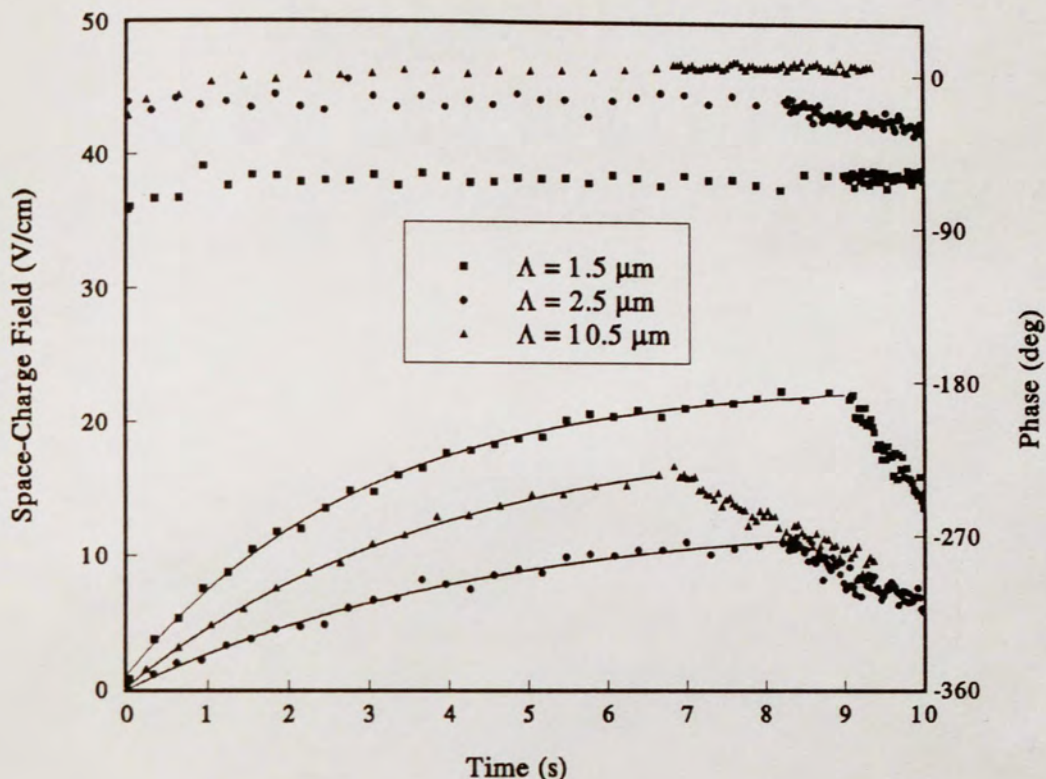


**Figure 6.7**  
Amplitude and Phase in  $\text{KNbO}_3:\text{Fe}$   
as a Function of Spatial Frequency

There is clearly a photovoltaic field in  $\text{KNbO}_3:\text{Fe}$ , and the crystal phase shows a spatial dependence similar to that of  $\text{BaTiO}_3$ . The amplitude and phase data conflict. The phase shows the effects of an increased diffusion field at the higher spatial frequencies, but this is not reflected in the amplitude. As seen in the summary table shown below, the results for  $\text{KNbO}_3:\text{Fe}$  were inconsistent at all spatial frequencies.

TABLE 6.5  
MEASURED FIELD PARAMETERS FOR KNbO<sub>3</sub>:Fe

$\Lambda$ ( $\mu\text{m}$ )	$\Delta n$ ( $\times 10^{-6}$ )	$E_{\text{sc}}$ (V/cm)	$\Delta E_{\text{sc}}$ (%)	$\eta$ (%)	$\phi$ (deg)	$\Delta\phi$ ( $\pm$ deg)	$\tau_{\text{eff}}$ (s)	$\Delta\tau_{\text{eff}}$ /(%)
1.5	.56	17	30	.03	51	15	2.2	10
2.5	.40	12	25	.02	33	18	3.2	30
10.5	.69	21	40	.04	5	20	4.7	70

In summary, results for KNbO<sub>3</sub>:Ta and BaTiO<sub>3</sub> were very good. LiNbO<sub>3</sub>:Fe showed strong fields, but will require future experiments more closely designed around its particular characteristics. KNbO<sub>3</sub>:Fe showed very poor results.

The major system problem was the frequency stability of the sweep oscillator. The frequency had a tendency to drift in an unpredictable manner. The phase-matching requirements at both Bragg cells, coupled with the fact that the angular deflection of the diffracted beam from the second Bragg cell directly effects the spatial light pattern in the crystal, underline the need for a stable frequency source. For some runs, the effect of the source instability was evident and the run was repeated. In other cases, the effect of the drift was not evident until the data were linearized from the log scale. It is thought that a more stable source will improve the results, particularly in slower materials. It should be mentioned



that this experiment was the first comprehensive test of this measurement technique. Overall, the system performed very well during this initial data run.

## CHAPTER 7

### DETERMINATION OF MATERIAL PROPERTIES

In this chapter, the grating parameters presented in Chapter 6 are used to calculate the following material properties: drift and diffusion transport lengths  $L_D$  and  $L_{ph}$ , Debye screening length  $l_s$ , effective trap density  $N_T$ , the product of mobility and carrier lifetime  $\mu\tau$ , and the product of the fractional poling factor and net conductivity  $F\bar{\sigma}$ . The methods for calculation of these properties is discussed, followed by presentation of the calculated material properties and summarizing comments.

#### Analytic Methods

Both the short-time limit and saturation models for the space-charge fields are utilized in the data analysis. In the short-time limit, the amplitude has a linear dependence, shown by equation (3.13), page 13. In the experiment it was not feasible to interrupt grating formation for a series of sufficiently short periods to measure the grating response during the short-time limit. Nevertheless, there is measured data applicable to this time period. Recall that the measured data were fit to equation (3.29), page 18, where the measured saturation amplitude and time information was used to solve for the effective time constant. Taking the derivative

of both equations, (3.13) and (3.29), for small  $t$ , and equating the two models gives, for each spatial frequency,

$$\frac{E_{sc}(z)}{\tau_{eff}} = \frac{qg_o m}{\epsilon [1 + (KL_{ph})^2]^{\frac{1}{2}}} \left[ L_{ph} \cos(Kz - \phi_{ph}) + \frac{KL_D^2}{1 + (KL_D)^2} \sin(Kz - \phi_{ph}) \right]. \quad (7.1)$$

It is assumed that  $m$ ,  $g_o$ , and  $\epsilon$  were constant for the three spatial frequencies. The modulation  $m$  was controlled experimentally, and it was kept  $> .99$  for all runs. Using the measured values for  $E_{sc}(z)$  and  $\tau_{eff}$  at  $1.5 \mu\text{m}$  as a standard, division of that slope by the slopes at each of the other spatial frequencies results in two amplitude equations for the two unknowns  $L_D$  and  $L_{ph}$ .

The phase also may be expressed in terms of the transport lengths. The phase relation in equation (3.13), page 18, can be simplified and related to the measured data by

$$\phi_m = \phi_{ph} + \Phi, \quad (7.2)$$

where  $\phi_m$  is the measured field phase and

$$\Phi = \tan^{-1} \frac{KL_D^2}{L_{ph} [1 + (KL_D)^2]}. \quad (7.3)$$

Recall that  $\phi_{ph} = \tan^{-1}(KL_{ph})$ . Here are three equations for the two unknowns  $L_D$  and  $L_{ph}$ . Considering both the phase and amplitude measurements, it is clear that there is an abundance of data available for solution of the two unknowns. It is desirable to use all of the measured information available. Accordingly, values of  $L_D$  and  $L_{ph}$  were recursed in the five equations of (7.1) and (7.2) until the total difference between the measured data and the theoretical models was minimum. Having  $L_D$ , the  $\mu\tau$  product may be calculated.  $L_D$  was

defined in equation (3.14), page 13, as  $L_D = (\tau D)^{1/2}$ . Use of the Einstein relation,  $D = \mu k_B T / q$ , yields the  $\mu\tau$  product,

$$\mu\tau = \frac{qL_D^2}{k_B T}. \quad (7.4)$$

Estimation of  $\tau$  is not attempted here. The high resistivity of oxide crystals renders mobility measurements difficult, and published results for mobilities, where available [19,31], can vary by as much as a factor of  $10^4$  for a single crystal type.

The saturation data were treated in much the same manner as those of the short-time limit, in that all measured data were used in the analysis. It should be noted that this discussion on analytical methods is presented in the chronological order in which the various operations were performed. It is obvious that the saturation and short-time models are related, and the order of operations is not critical. For the saturation analysis, reference is made to equations (3.27) and (3.28), page 17. The saturation equations were used to solve for  $F\bar{\sigma}$ , defined in equation (3.26), page 16, and the screen field  $E_q$ , defined in equation (3.24), page 16. Values of  $\bar{\sigma}$  and  $E_q$  were recursed through the three saturation amplitude and three phase equations, solving at values of minimum error between the measured data and the model. From  $E_q$ , calculations of  $N_T$  and  $l_s$  were made via equation (3.23), page 15, and equation (3.25), page 16, respectively.

### Material Properties

The numerical analyses outlined in the previous section were performed with the measured data shown in Chapter 6 for the  $\text{KNbO}_3:\text{Ta}$ ,  $\text{BaTiO}_3$ ,  $\text{KNbO}_3:\text{Fe}$ , and  $\text{LiNbO}_3:\text{Fe}$  crystals. The results for  $\text{BaTiO}_3$  and  $\text{KNbO}_3:\text{Ta}$  are very good. The measured data for

KNbO<sub>3</sub>:Fe and LiNbO<sub>3</sub>:Fe showed poor consistency, and comparison of the measured data with the models revealed very little. Consequently, none of the material properties could be found for LiNbO<sub>3</sub>:Fe and KNbO<sub>3</sub>:Fe. Table 7.1 contains the calculated material properties for KNbO<sub>3</sub>:Ta and BaTiO<sub>3</sub>.

TABLE 7.1  
MATERIAL PROPERTIES

CRYSTAL	$L_D$ (nm)	$L_{ph}$ (nm)	$N_T$ ( $10^{16}cm^{-3}$ )	$l_s$ ( $\mu m$ )	$\mu\tau$ ( $10^{-9}cm^2/V$ )	$F\bar{\sigma}$
BaTiO <sub>3</sub>	100	7	1.3	.75	3.9	.20
KNbO <sub>3</sub> :Ta	150	0	.27	1.1	8.7	.26

In BaTiO<sub>3</sub>, both the 1.5 and 2.5  $\mu m$  amplitudes converged to within 1% of the saturation model prediction for the values of  $\bar{\sigma}$  and  $N_T$  shown in the table. The saturation phases for BaTiO<sub>3</sub> differed from the model by less than 2° at 1.5 and 2.5  $\mu m$ , and less than 3° at 10.5  $\mu m$ . All three phase values were within 4° of the phase predicted by the short-time model. Figure 7.1, below, shows the experimental amplitude and phase compared to the model.

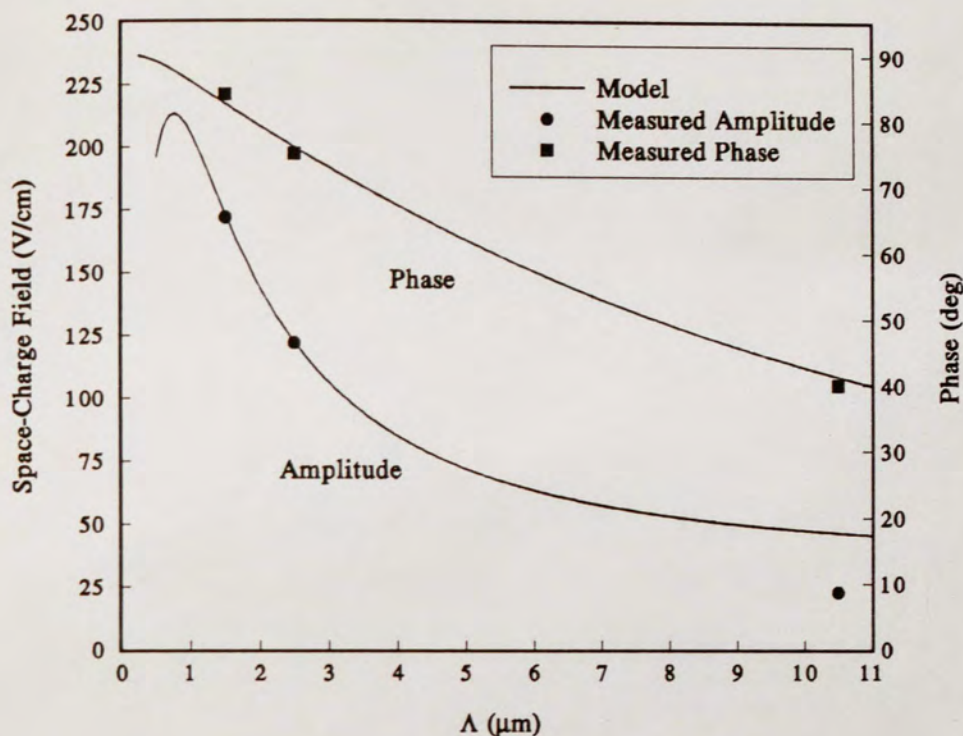


**Figure 7.1**  
Comparison of Experimental Data and Theoretical Model  
for  $\text{BaTiO}_3$  as a Function of Spatial Frequency

The amplitude performance for  $\text{KNbO}_3:\text{Ta}$  was similar to that of  $\text{BaTiO}_3$ , with clear convergence with the saturation model for the parameters listed in the table. The measured and theoretical phase of  $\text{KNbO}_3:\text{Ta}$  differed by less than  $1^\circ$  at 1.5 and 2.5  $\mu\text{m}$ , and displayed a  $4^\circ$  difference at 10.5  $\mu\text{m}$ . A perplexing feature of the analysis is that the amplitude of the 10.5  $\mu\text{m}$  data for  $\text{KNbO}_3:\text{Ta}$  and  $\text{BaTiO}_3$  did not reach the amplitude levels predicted by the models, while the data at 1.5 and 2.5  $\mu\text{m}$  clearly indicated the parameters listed in the table. A plausible explanation is dependence of  $\bar{\sigma}$  on spatial frequency. Figure 7.2, below, shows the experimentally measured amplitude and phase of  $\text{KNbO}_3:\text{Ta}$  compared to the model.

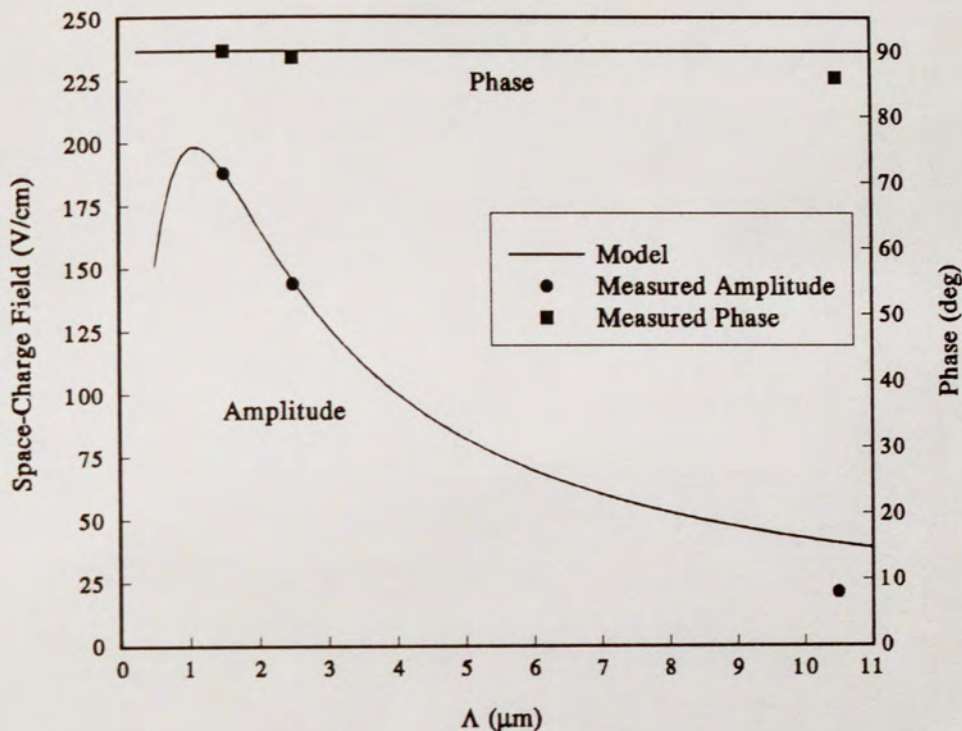


**Figure 7.2**  
Comparison of Experimental Data and Theoretical Model  
for  $\text{KNbO}_3:\text{Ta}$  as a Function of Spatial Frequency

Some of the spread in the amplitude data may be due to variation over time of the diffraction efficiency of the second Bragg cell. This parameter was measured frequently during data acquisition sessions, and confidence in its value is given at  $\pm 3\%$ . In conversion of the measured data to a linear scale, the percent error in the space-charge field depends on the actual field strength. See equation (5.32), page 39, where  $\tan(\gamma_2)$  is the factor in question. For the maximum saturation values of  $\text{KNbO}_3:\text{Ta}$  and  $\text{BaTiO}_3$ ,  $\pm 3\%$  variation in diffraction efficiency,  $\eta = \sin^2(\gamma_2)$ , leads to an error in the field amplitude of  $\pm 7\%$ . For a typical saturation field in  $\text{LiNbO}_3:\text{Fe}$ , the error increases to about  $\pm 10\%$ . The variation in the

diffraction efficiency appeared to be random, and over several runs would tend to average out. The variation in the diffraction efficiency is most likely due to a combination of frequency drift and instability of the variable attenuator shown in Figures 4.1 and 4.2.

This explanation does not account for the low amplitudes mentioned regarding the 2.5  $\mu\text{m}$  data for  $\text{BaTiO}_3$  and  $\text{KNbO}_3:\text{Ta}$  in the previous section. This doubt in the 2.5  $\mu\text{m}$  amplitudes is compounded by the fact that these data were taken with the configuration of Figure 4.2, while all 1.5 and 2.5  $\mu\text{m}$  data were taken using the configuration of Figure 4.1. A satisfactory conclusion has not been reached.

### Summary

Overall, the experimental system is found to be an excellent tool for characterization of photorefractive crystals. The grating characteristics presented in Chapter 6 are valuable for determination of the appropriate material for a particular application, and knowledge of the material properties can serve as a feedback mechanism for those involved with the manufacture of photorefractive crystals. A logical extension of this work is modification of the experimental system for characterization of semiconductor photorefractive materials, where the fabrication technology is more advanced and the grating response time can be orders of magnitude faster than those reported here.



## REFERENCES

- [1] Yariv, Amnon, and Yeh, Pochi. Optical Waves in Crystals. Wiley Series in Pure and Applied Optics. New York: John Wiley and Sons, 1984.
- [2] Bragg cell parameters courtesy of Dr. Robert Montgomery, Harris Corporation. Melbourne, Florida.
- [3] Sherman, Christopher J.. "Implementation and Analysis of an Acousto-Optic Photorefractive Correlator." Masters Thesis, University of Central Florida, 1990.
- [4] Berg, Norman J., and Lee, John N.. Acousto-Optic Signal Processing: Theory and Implementation. Optical Engineering Series, vol. 2. New York: Marcel Dekker, 1983.
- [5] Moharam, M.G., Gaylord, T.K., and Magnusson, R.. "Criteria for Bragg Regime Diffraction by Phase Gratings." Optics Communications 32 (January 1980): 14-18.
- [6] Gunter, P., ed. Electro-optic and Photorefractive Materials. Springer Proceedings in Pure and Applied Optics. New York: John Wiley and Sons, 1984.
- [7] Gottlieb, Milton, Ireland, Clive L.M., and Ley, John Martin. Electro-Optic and Acousto-Optic Scanning and Deflection. Optical Engineering Series, vol. 3. Marcel Dekker, 1983.
- [8] Valley, George C.. "Simultaneous Electron/Hole Transport in Photorefractive Materials." Journal of Applied Physics 59 (15 May 1986):3363-3366.
- [9] Gunter, P., and Huignard, J., eds. Photorefractive Materials and Their Applications I. Topics in Applied Physics, vol. 61. New York: Springer-Verlag, 1988. "Theory of Photorefractive Effects in Electro-optic Crystals," by George C. Valley and Juan F. Lam.
- [10] Strohkendl, F.P., Johnathan, J.M.C., and Hellwarth, R.W. "Hole-Electron Competition in Photorefractive Gratings." Optics Letters 11, no. 5 (May 1986): 312-314.
- [11] Moharam, M.G., Gaylord, T.K., and Magnusson, R.. "Holographic Grating Formation in Photorefractive Crystals with Arbitrary Transport Lengths." Journal of Applied Physics 50 (Sept. 1979): 5642-5651.

- [12] Valley, George C., and Klein, Marvin B.. "Optimal Properties of Photorefractive Materials for Optical Data Processing." Optical Engineering 22, no. 6 (November/December 1983): 704-711.
- [13] Kukhtarev, N.V.. "Kinetics of Hologram Recording and Erasure in Electrooptic Crystals." Sov. Tech. Phys. Lett 2, no. 12 (December 1976): 438-440.
- [14] Kukhtarev, N.V., Markov, V.B., Odulov, S.G., Soskin, M.S. and Vinetski, V.L. "Holographic Storage in Electro-Optic Crystals." Ferroelectrics 22 (1979): 949-960.
- [15] Rupp, R.A., Maillard, A., Walter, J.. "Impact of the Sublinear Conductivity Law on the Interpretation of Holographic Results in BaTiO<sub>3</sub>." Applied Physics A 49 (1989): 259-268.
- [16] Medrano, C., Voit, E., Amrhein, P., and Gunter, P.. "Optimization of the Photorefractive Properties of KNbO<sub>3</sub> Crystals." Journal of Applied Physics 64, no. 9 (1 November 1988): 4668-4673.
- [17] Klein, M.B., and Valley, George C.. "Beam Coupling in BaTiO<sub>3</sub> at 442 nm." Journal of Applied Physics 57, no. 11 (1 June 1985): 4901-4905.
- [18] Zha, M.Z., Amrhein, P., and Gunter, P.. "Measurement of the Phase Shift of Photorefractive Gratings by a Novel Method." IEEE Journal of Quantum Electronics 26, no. 4 (April 1990): 788-792.
- [19] Gunter, P., and Huignard, J., eds. Photorefractive Materials and Their Applications I. Berlin, Springer-Verlag, 1988. "Photorefractive Properties of BaTiO<sub>3</sub>," by Marvin B. Klein.
- [20] Gunter, P.. "Holography, Coherent Light Amplification and Optical Phase Conjugation with Photorefractive Materials." Physics Reports 93, no. 4 (1982): 199-299.
- [21] Makgerefteh, Daniel, and Feinburg, Jack.. "Erasure Rate and Coasting in Photorefractive Barium Titanate at High Optical Power." Optics Letters 13, no. 12 (December 1988): 1111-1113.
- [22] Gunter, P., and Huignard, J., eds. Photorefractive Materials and Their Applications I. Berlin, Springer-Verlag, 1988. "Photorefractive Measurements of Physical Parameters," by Ruth A. Mullen.
- [23] Feinburg, J., Heiman, D., Tanguay, A.R., Jr., and Hellwarth, R.W.. "Photorefractive Effects and Light-induced Charge Migration in Barium Titanate." Journal of Applied Physics 51, no. 3 (March 1980): 1297-1305.

- [24] Valley, G.C.. "Two-Wave Mixing with an Applied Field and Moving Grating." Journal of the Optical Society of America B 1, no.6 (December 1984): 868-873.
- [25] Refreiger, P.H., Solymar, L., Rajenbach, H., and Huignard, J.P.. "Two-beam Coupling in Photorefractive  $\text{Bi}_{12}\text{SiO}_{20}$  Crystals with Moving Grating: Theory and Experiments." Journal of Applied Physics 58, no. 1 (July 1985): 45-57.
- [26] Montgomery, R.M., and Lange, M.R.. "Amplitude and phase measurement technique for photorefractive gratings." Journal of Applied Physics 68, no. 9 (1 November 1990): 4782-4787.
- [27] Chang, I.C.. "Selection of Materials for Acousto-Optic Devices." Optical Engineering 24, no. 1 (January/February 1985): 132-137.
- [28] Seymour, Robert S.. "Acoustooptic Bragg Diffraction in Anisotropic Optically Active Media." Applied Optics 29 (20 February 1980): 822-826.
- [29] Warner, A.W., White, D.L., and Bonner, W.A.. "Acousto-Optic Light Deflectors Using Optical Activity in Paratellurite." Journal of Applied Physics 43 (November 1972): 4489-4495.
- [30] Kogelnik, Herwig. "Coupled Wave Theory for Thick Hologram Gratings." The Bell System Technical Journal 48, no. 9 (November 1969): 2909-2945.
- [31] Gunter, P., and Huignard, J., eds. Photorefractive Materials and Their Applications I. Berlin, Springer-Verlag, 1988. "The Photorefractive Effect in Semiconductors," by Ruth A. Mullen.